AN ABSTRACT OF THE THESIS OF

River Alan Wiedle for the degree of Honors Baccalaureate of Science in Physics presented on May 16, 2013. Title: Thermal conductivity measurements of amorphous thin films on silicon via the 3ω method

Abstract approved: ______________________________

Janet Tate

Thermal transport properties of a material are often difficult to measure, especially for thin films, but they are important for materials that have applications in modern devices, such as nano-scale electronics, thermoelectrics, and thermally resistive coatings. In this thesis, we describe an apparatus developed to measure the thermal conductivity of bulk and thin film materials via the 3ω method and a procedure to construct the high quality microheaters needed for the measurement process. The theoretical basis of the 3ω method is derived in detail and we demonstrate how thermal properties are extracted from experimental data. To test the validity of the method, we measure the thermal conductivity of bulk Corning 1737 glass, a well established thermal standard; results indicate that the conductivity is 0.90 W m^{-1} K^{-1}, consistent with the known value to within 2%. We also test the thermal conductivity of two types of bulk silicon and show that the thermal conductivity is strongly dependent on doping concentration. Amorphous aluminum phosphate (AlPO) films are also characterized; this material has potential use in microelectronics as nanometer-scale, high quality insulating films can be created with an all-aqueous spin coating technique. We show that AlPO films with thickness 50-200 nm have a thermal conductivity of 0.94(3) W m^{-1} K^{-1}, comparable to other dielectrics currently used in the microelectronics industry.

Key Words: Thermal conductivity, interface resistance, 3ω method, amorphous dielectric, thin-film, AlPO, solution process, silicon

Corresponding Email Address: wiedler@onid.orst.edu

©Copyright by River Alan Wiedle
May 16, 2013
All Rights Reserved

Thermal conductivity measurements of amorphous thin films on silicon via the 3ω method

by

River Alan Wiedle

A PROJECT

submitted to

Oregon State University

University Honors College

in partial fulfillment of
the requirements for the
degree of

Honors Baccalaureate of Science in Physics (Honors Scholar)

Presented May 16, 2013
Commencement June 2013

Honors Baccalaureate of Science in Physics project of River Alan Wiedle presented on May 16, 2013

APPROVED:

Mentor, representing Physics

Committee Member, representing Physics

Committee Member, representing Physics

Chair, Department of Physics

Dean, University Honors College

I understand that my project will become part of the permanent collection of Oregon State University, University Honors College. My signature below authorizes release of my project to any reader upon request.

River Alan Wiedle, Author

ACKNOWLEDGEMENTS

I am forever indebted to all who have worked with me on this project. First, I thank my mentor, Dr. Janet Tate, for her guidance and encouragement in both academics and research. Janet has given me a great deal of freedom in this project and the opportunity to fully explore the often gory, yet exciting and enlightening details of experimental physics. I especially thank Mark Warner; his experience in electronics design and troubleshooting, as well as his commitment to this project, were invaluable. Without Mark, this project may have ended before it truly began, as it was his efforts that led to the creation of the circuitry used to extract the 3ω signal. Thanks to David McIntyre for his academic advising over the years and for the many discussions we have had regarding working the bugs out of this experiment. Thanks to Paul Plassmeyer and the Page lab at the University of Oregon for providing the AlPO samples and x-ray reflectivity measurements used in this thesis. Also thanks to the many others who have been involved with this project, including Matt Oostman, Nicola Schmidt, and all other members of the Tate lab.

Thanks to the McIntyre and Hetherington labs for providing test equipment used in these measurements, to the Materials Synthesis and Characterization Facility (MaSC) for use of their clean room and photolithography tools, to the Microproducts Breakthrough Institute (MBI) for creation of the shadow masks used to deposit our first microheaters, and to the Keszler lab for use of their ellipsometry equipment and for producing samples for our initial thin film measurements.

Funding for this project was provided by the Oregon State University URISC program, the Center for Sustainable Materials Chemistry, and NSF CHE-110263. Thank you for all of your support!

TABLE OF CONTENTS

Page

1. INTRODUCTION 1
   - 1.1. Thermal Transport Properties 1
   - 1.2. The Origin of the 3-omega Method 2
   - 1.3. Scope of This Thesis 3
2. THE 3ω METHOD 4
   - 2.1. The 3ω geometry 4
   - 2.2. The 1D Heater Solution 6
   - 2.3. The 2D Heater Solution 11
   - 2.4. Parameters of the 2D Heater Model 16
   - 2.5. The Thin Film Approximation 21
   - 2.6. Measuring the Temperature: The 3ω Voltage 24
3. EXPERIMENTAL APPARATUS 27
   - 3.1. Heater Design 27
   - 3.2. Measurement System 33
     - 3.2.1 Subtraction Circuit 34
     - 3.2.2 Lock-in Amplifier and Automation 37
     - 3.2.3 Substrate Heating 40
     - 3.2.4 Electrical Contact to Heater 42
     - 3.2.5 Sample Holder 43
4. EXPERIMENTAL RESULTS 45
   - 4.1. Calibration with 1737 45
   - 4.2. Effects of Doping on Si 46

TABLE OF CONTENTS (Continued)

Page

4.3. AlPO Thin Films 49

4.3.1 Sample Preparation 49

4.3.2 Thermal Conductivity Results 51

5. CONCLUSIONS 55

BIBLIOGRAPHY 58

LIST OF FIGURES

Figure		Page
2.1	Temperature rise of the microheater over time.	6
2.2	Geometry of the 1D heater.	8
2.3	Zeroth order hyperbolic Bessel functions of first and second kinds.	10
2.4	Cross section of the 2D heater on substrate geometry.	12
2.5	Modeled temperature *vs.* frequency curve for the 2D heater geometry.	15
2.6	Thermal penetration depth *vs.* current frequency.	18
2.7	Effects of the substrate thermal diffusivity on the 2D heater model.	19
2.8	Effects of the substrate thermal conductivity on the 2D heater model.	19
2.9	Effects of the heater width on the 2D heater model.	20
2.10	The thin film on substrate geometry.	21
2.11	Heat flow through a thin film	22
2.12	Effects of adding a thin film to the 2D heater model.	23
3.1	Two and four contact pads designs of the 3ω heater.	28
3.2	Simulated temperature rise along the length of a heater with two contact pads.	29
3.3	Electrical resistivity *vs.* temperature coefficient of resistance for several metals.	30
3.4	Diagrams of the lift-off photolithography process.	32
3.5	Microscope images of a 20-μm and a 5-μm wide heater produced by the photolithography process.	33
3.6	Schematic of the subtraction circuit.	35
3.7	Transfer function of an INA128P amplifier.	37
3.8	Functional schematic of the LabVIEW automation program.	41
3.9	Diagram of the sample mount.	44

LIST OF FIGURES (Continued)

Figure Page

4.1 Thermal resistance *vs.* current frequency for a measurement on a 1737 substrate 46

4.2 Thermal resistance *vs.* current frequency for n-Si and p-Si. 47

4.3 Electrical resistivity *vs.* carrier density for n-Si and p-Si. 49

4.4 Ellipsometry measurements on layered AlPO films. 50

4.5 Thickness *vs.* number of layers of the 450°C and 600°C annealed AlPO films. 51

4.6 XRR measurement on a single layer AlPO film. 52

4.7 Thermal resistance *vs.* current frequency for a series of AlPO films. 53

1. INTRODUCTION

1.1. Thermal Transport Properties

The thermal conductivity κ is an important material property in modern physics. It appears in the law of thermal conduction (sometimes called Fourier's Law), which relates the heat flux density $\vec{Q}$ to a temperature gradient ∇T:

$$\vec{Q} = -\kappa \nabla T. \tag{1.1}$$

In addition, the thermal conductivity of a material is related to other thermal parameters by the equation

$$\kappa = \rho C_p D, \tag{1.2}$$

where ρ is the density, C_p is the specific heat capacity, and D is the thermal diffusivity. The thermal diffusivity describes how quickly heat spreads out in a medium and is the relevant parameter in the heat equation:

$$\frac{\partial T}{\partial t} = D \nabla^2 T. \tag{1.3}$$

In the microelectronics industry, thermal transport properties play a key role in the efficiency and lifetime of devices. Generally, faster electronics use more power, dissipating more waste heat that must be removed from the system. As devices decrease in size and increase in speed, new materials must be created to lower the thermal resistance of a system and promote fast heat diffusion. This is typically done by increasing the thermal conductivity of materials used and by minimizing thermal resistance at interfaces between materials.

In other applications, materials of low thermal conductivity are of particular interest.

For example, in thermoelectric devices, the thermal conductivity plays a key role in the figure of merit

$$ZT = \frac{\sigma S^2 T}{\kappa}, \tag{1.4}$$

where σ is the electrical conductivity and S is the thermopower (also called the Seebeck coefficient). As a larger figure of merit leads to a high thermoelectric efficiency, much work goes into increasing the electrical conductivity of a material while simultaneously decreasing its thermal conductivity [1]. In practice, this is difficult as the ratio σ/κ is typically independent of the material itself, as shown by the famous Wiedemann-Franz law [2]. In thermal insulators, a low thermal conductivity is clearly desirable. However, it is difficult to achieve extremely low thermal conductivities for solid materials (the most insulating glasses are around 1 W m^{-1} K^{-1}). Lower thermal conductivities are achieved in a variety of ways, such as by introducing structural defects and thermal interfaces into a material [1, 3] Of particular interest are a class of materials called nanolaminates: alternating layers of different materials that can be produced in such a way that each individual layer is both very smooth and very thin. Thermal interfaces are created between each layer; as such, nanolaminates can be used to make very low thermal conductivity structures. Amorphous dielectrics such as aluminum phosphate (AlPO), hafnium and zirconium sulfates, and amorphous metals (such as ZrCuAlNi and TiAl) have been of recent interest as nanolaminates useful in nanoelectronics and other applications [3].

1.2. The Origin of the 3-omega Method

The modern 3ω method was developed in the late 1980s by Cahill and Pohl [4]. This technique draws heavily on the work of Birge and Nagel, who measured the specific heat capacity of liquids using a "heat spectrometer" consisting of a thin, planar heater immersed in the liquid [5, 6]. Cahill's method uses a similar circuit and heater design to

measure the thermal conductivity of bulk materials and thin films [7]. He also developed a differential version of the technique to study thin films [8]. Kim *et al.* [9] derives a model useful for the analysis of layered films and improves on Cahill's method by showing how to eliminate the effects of parasitic thermal interfaces from the measurement. Other authors have implemented additional changes to the technique and analysis methods, taking into account finite substrate thickness [10], thermal conduction along the heater and heater length effects [9, 11, 12], film anisotropy [13], high frequency variations [14], and other complicated effects. Jaquot *et al.* have developed 3ω heaters using a spiral geometry; many of these heaters can be conveniently deposited onto Kapton tape; individual heaters can then be places onto samples [15]. However, this technique has limited application for thin film measurements due to the additional thermal resistance of the Kapton film and the additional interfaces that are difficult to characterize.

1.3. Scope of This Thesis

This paper presents an overview of the physics behind the 3ω method and a derivation of the model created by Cahill [7] for measurements on bulk materials and a simple extension of this model for thin film on substrate geometries. Effects of changing the geometry of the experiment's heat source/temperature probe and material characteristics is examined. The system built to perform the 3ω measurement is described in detail, along with the photolithography procedures used to deposit the measurement probes onto the samples. A calibration of the system using Corning 1737 bulk glass is shown and the results are compared to the well established thermal properties of this material. Experimental data on two types of silicon substrates with different doping concentrations are presented. Results on a series of novel amorphous aluminum phosphate (AlPO) films deposited by an aqueous spin-coating technique are also presented.

2. THE 3ω METHOD

2.1. The 3ω geometry

The measurement probe for the 3ω method consists of a thin metal strip in intimate thermal contact with the sample. This probe serves both as the heat source for the measurement and the thermometer. In the simplest geometry, the probe (henceforth called the heater) is rectangular having length l and half-width b. In this derivation, the thickness of the heater and the geometry of the electrical contact pads is ignored. When an electrical current of frequency ω and magnitude I_0 given by

$$I(t) = I_0 \cos \omega t \tag{2.1}$$

is applied to the heater, power is dissipated through the resistive heating process. Assuming that the change in resistance, ΔR, of the heater caused by the resulting temperature increase is small compared to its resistance at ambient temperature R_0, the power dissipated by the heater is

$$\begin{aligned} P(t) =& I(t)^2 R_0 \\ =& I_0^2 R_0 \cos^2(\omega t) \\ =& \frac{1}{2} I_0^2 R_0 + \frac{1}{2} I_0^2 R_0 \cos(2\omega t). \end{aligned} \tag{2.2}$$

Equation 2.2 shows that there are two components to the dissipated power. We define these components as

$$P_{DC} = \frac{1}{2} I_0^2 R_0 \tag{2.3}$$

$$P_{AC}(t) = \frac{1}{2} I_0^2 R_0 \cos(2\omega t). \tag{2.4}$$

The first component, P_{DC} does not vary with time. The second component, P_{AC} has the same magnitude as P_{DC}, but oscillates with twice the frequency of the applied current. The heat flux generated by the heater is proportional to the average power:

$$\begin{aligned}\langle P\rangle =& \frac{\omega}{\pi}\int_0^{\pi/\omega} P(t)dt \\ =& \frac{1}{2}I_0^2R_0.\end{aligned} \tag{2.5}$$

Note that the average power is related to the root mean squared current and voltage by

$$\langle P\rangle = I_{rms}V_{rms}. \tag{2.6}$$

It is clear from Equation 2.5 that the AC power does not contribute to the average power. This implies that once the system reaches a steady state condition, the AC and DC temperature profiles are independent.

The power dissipated by the heater causes the temperature of the heater to rise. The magnitude and phase (relative to the driving current) of this temperature rise is determined by material properties and geometry of the heater and its surroundings. Since there are both constant and oscillating components of the power, there is a constant and oscillating rise to the temperature (see Figure 2.1.). We define the temperature rise in the substrate above ambient at the spatial coordinate $\vec{r}$ as

$$\Delta\Theta(\vec{r},t) = \Delta\Theta_{AC}(\vec{r})\theta(t) + \Delta\Theta_{DC}(\vec{r}) \tag{2.7}$$

$\Delta\Theta(\vec{r},t)$ is a complex function and it is understood that the temperature is the real part of $\Delta\Theta(\vec{r},t)$. Furthermore, we assume that the oscillating part of the temperature can be separated into its space- and time-like components $\Delta\Theta_{AC}(\vec{r})$ and $\theta(t)$. Since the temperature rise is caused by power dissipation at 2ω, the frequency of the temperature oscillations (often called the heating frequency) is 2ω. Therefore, the time dependence of

the heater is given by

$$\theta(t) = e^{i2\omega t}. \tag{2.8}$$

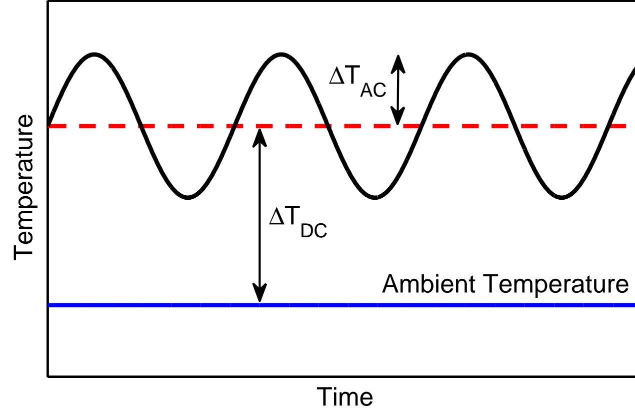

FIGURE 2.1: Temperature rise of the microheater over time.

2.2. The 1D Heater Solution

The important quantity in the 3ω method is the temperature of the heater and the phase of this temperature, relative to the current oscillations. To simplify this calculation, we first assume that the heater is an infinite line heater embedded onto the surface of a substrate of thermal conductivity κ and thermal diffusivity D. As shown in Figure 2.2, the surface of this substrate is oriented in the xz-plane and is infinite in the region below this plane. The heater is oriented along the z-axis. We begin this derivation by modeling the heater as a half cylinder with radius a and later take the limit where $a \to 0$. We assume that heat does not propagate upward (the thermal conductivity of the region above the surface has a small conductivity compared to the material). In this geometry, heat only propagates radially outward from the curved surface of the heater; therefore, the

temperature depends only on the radial coordinate r (defined only below the xz-plane). As a boundary condition, we force the magnitude of the temperature rise to decay to zero far away from the heater ($\Delta\Theta_{AC}(r = \infty) = \Delta\Theta_{DC}(r = \infty) = 0$). The thermal conductivity is included in the model through a second boundary condition, namely that the heat flux through the substrate is equal to the power dissipated by the heater, as shown by Fourier's law. To begin, we restate the heat equation:

$$\nabla^2 \Delta\Theta = \frac{1}{D}\frac{\partial \Delta\Theta}{\partial t}. \tag{2.9}$$

Since $\Delta\Theta = \Delta\Theta(r, t)$, this reduces to

$$\frac{1}{r}\frac{\partial}{\partial r}\left(r\frac{\partial \Delta\Theta(r,t)}{\partial r}\right) = \frac{1}{D}\frac{\partial \Delta\Theta(r,t)}{\partial t}. \tag{2.10}$$

By expanding $\Delta\Theta$ in terms of its constant and oscillating parts, Equation 2.10 becomes

$$\begin{aligned}\frac{1}{r}\frac{\partial}{\partial r}\left(r\frac{\partial \Delta\Theta_{AC}(r)\theta(t)}{\partial r}\right) + \frac{1}{r}\frac{\partial}{\partial r}\left(r\frac{\partial \Delta\Theta_{DC}(r)}{\partial r}\right)\\ = \frac{1}{D}\left(\frac{\partial \Delta\Theta_{AC}(r)\theta(t)}{\partial t} + \frac{\partial \Delta\Theta_{DC}(r)}{\partial t}\right).\end{aligned} \tag{2.11}$$

Clearly, the time derivative of $\Delta\Theta_{DC}$ is zero. The spatial derivatives of $\Delta\Theta_{DC}$ also go to zero due to the independence of the constant and oscillating components of the temperature. To verify this, consider the case when the heater is supplied with only a DC current. The power dissipated has only a DC component and the heat flux density $\vec{Q}(\vec{r})$ has a radial component that decreases like $1/r^2$. Thus,

$$\vec{Q}(r) = \frac{Q_0}{r^2}\hat{r}. \tag{2.12}$$

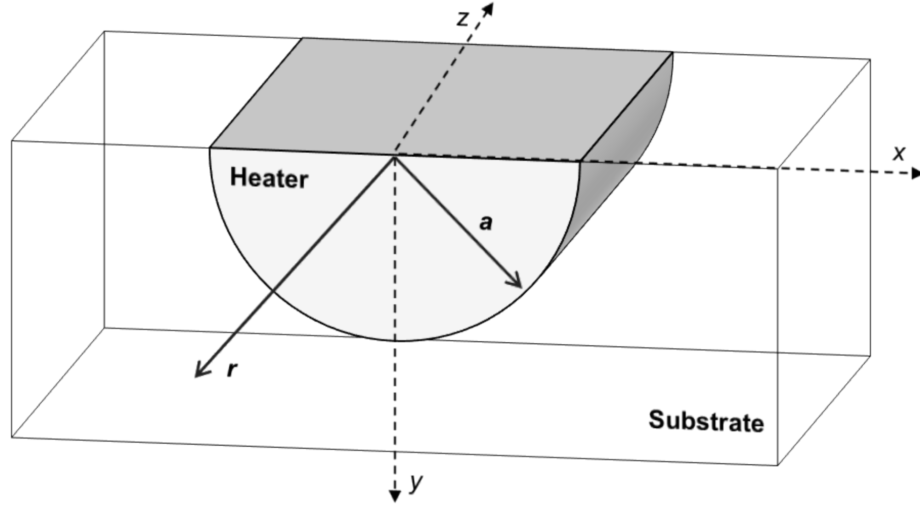

FIGURE 2.2: Geometry of the 1D heater. Heat flows radially outward from the surface of the heater in contact with the substrate. In the 1D model, we take the limit as the heater radius goes to zero.

In this example, Fourier's law becomes

$$\frac{Q_0}{r^2}\hat{r} = -\kappa \frac{d\Delta\Theta_{DC}(r)}{dr}\hat{r}. \tag{2.13}$$

Solving Equation 2.13 using the boundary condition $\Delta\Theta_{DC}(\infty) = 0$ yields

$$\Delta\Theta_{DC}(r) = \frac{Q_0}{\kappa}\frac{1}{r}. \tag{2.14}$$

Thus, the spatial derivative of $\Delta\Theta_{DC}$ in Equation 2.11 vanishes and the equation reduces to

$$\frac{1}{r}\frac{\partial}{\partial r}\left(r\frac{\partial\Delta\Theta_{AC}(r)\theta(t)}{\partial r}\right) = \frac{1}{D}\frac{\partial\Delta\Theta_{AC}(r)\theta(t)}{\partial t}. \tag{2.15}$$

Using $\theta(t)$ from equation 2.8, the time derivative is evaluated and $\theta(t)$ is divided out:

$$\frac{1}{r}\frac{\partial}{\partial r}\left(r\frac{\partial\Delta\Theta_{AC}(r)}{\partial r}\right) = \frac{i2\omega}{D}\frac{\partial\Delta\Theta_{AC}(r)}{\partial t}. \tag{2.16}$$

This is rewritten as

$$r^2 \frac{d^2 \Delta\Theta_{AC}(r)}{dr^2} + r\frac{d\Delta\Theta_{AC}(r)}{dr} - r^2 q^2 \Delta\Theta_{AC}(r) = 0, \tag{2.17}$$

where

$$q = \sqrt{\frac{i2\omega}{D}}. \tag{2.18}$$

Solutions to this differential equation are linear combinations of the zeroth order hyperbolic Bessel functions of first and second kinds, $I_0(qr)$ and $K_0(qr)$ [16]. Thus,

$$\Delta\Theta_{AC}(r) = c_1 I_0(qr) + c_2 K_0(qr). \tag{2.19}$$

As r increases, the temperature oscillations must decay to zero. As seen in Figure 2.2., I_0 tends toward infinity for large r, resulting in unphysical behavior, while K_0 approaches zero. Thus,

$$\Delta\Theta_{AC}(r) = c_2 K_0(qr). \tag{2.20}$$

In addition, we can calculate the heat flux using Fourier's law. Since the heat flux out of the heater is equal to the average power dissipated by the heater,

$$\frac{\langle P\rangle}{A} = -\kappa \frac{d\Theta_{AC}(r)}{dr}\bigg|_{r=a}. \tag{2.21}$$

Here, $A = \pi al$ is the surface area of the heater. Since $d/dr[K_0(qr)] = -qK_1(qr)$,

$$\langle P\rangle = c_2(\pi la)\kappa q K_1(qa). \tag{2.22}$$

In the line heater limit ($a \to 0$),

$$\langle P\rangle = \lim_{a\to 0} c_2(\pi la)\kappa q K_1(qa) = \pi l\kappa c_2. \tag{2.23}$$

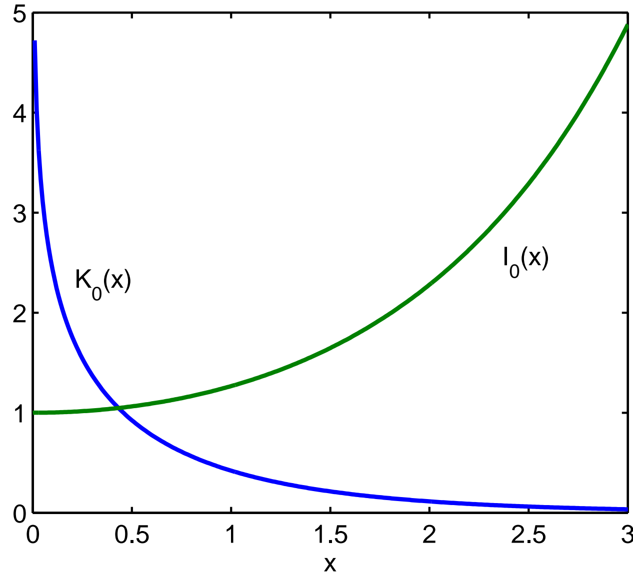

FIGURE 2.3: Zeroth order hyperbolic Bessel functions of first and second kinds.

Plugging c_2 into Equation 2.20 yields

$$\Delta\Theta_{AC}(r) = \frac{\langle P \rangle}{\pi l \kappa} K_0(qr). \tag{2.24}$$

In the limit where $|qr| << 1$, the first order expansion of $\Delta\Theta(r)$ is given by [16]

$$\Delta\Theta_{AC}(r) = \frac{\langle P \rangle}{\pi l \kappa} \left(\frac{1}{2} \ln \left(\frac{2D}{\omega r^2} \right) - \gamma - \frac{i\pi}{4} \right) \tag{2.25}$$

where $\gamma \approx 0.5772$ is the Euler-Mascheroni constant. From this equation, it is apparent that for sufficiently small ω (sufficiently small is determined in Section 3.3), the amplitude of the temperature decreases linearly with logarithmic ω. In addition, the temperature contains a frequency-independent imaginary part that corresponds to a temperature rise that is out-of-phase with the driving current. Physically, this corresponds to a time delay between the excitation current and the heating it causes. For convenience, we define the

phase shift as

$$\phi(\omega) = \arctan\left(\frac{\text{Im }\Theta_{AC}(\omega)}{\text{Re }\Theta_{AC}(\omega)}\right). \tag{2.26}$$

Thus, the real ("in-phase") and imaginary ("out-of-phase") parts of the temperature are

$$\Delta\Theta_{AC,x}(\omega) = |\Delta\Theta_{AC}(\omega)|\cos\phi \tag{2.27}$$

$$\Delta\Theta_{AC,y}(\omega) = |\Delta\Theta_{AC}(\omega)|\sin\phi \tag{2.28}$$

It is useful to take the derivative of the in-phase temperature with respect to $\ln(\omega)$:

$$\frac{d\Delta\Theta_{AC,x}(\omega)}{d\ln(\omega)} = -\frac{\langle P\rangle}{2\pi l\kappa}. \tag{2.29}$$

This suggests that if we can measure the in-phase temperature over a range of frequencies, we can determine the thermal conductivity of the substrate by the equation

$$\kappa = -\frac{\langle P\rangle}{2\pi l}\left(\frac{d\Delta\Theta_{AC,x}(\omega)}{d\ln(\omega)}\right)^{-1}. \tag{2.30}$$

Also, from 2.25, the magnitude of the out-of-phase temperature can be used to determine the thermal conductivity by the equation

$$\kappa = -\frac{\langle P\rangle}{4l\Delta\Theta_{AC,y}}. \tag{2.31}$$

2.3. The 2D Heater Solution

Next, we expand on the 1D heater temperature solution to include the effects of the finite width of the heater. Figure 2.4 shows the geometry for this derivation. While the heater is still of semi-infinite extent, it now rectangular (in the plane of the substrate) with a width of $2b$. As the heater is used to measure the temperature oscillations, we

care only about the temperature at the surface of the substrate ($y = 0$). To construct

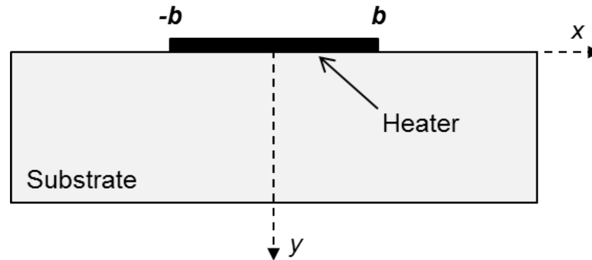

FIGURE 2.4: Cross section of the 2D heater on substrate geometry. The length of the heater extends into the page and is of infinitesimal width. The substrate is infinite in the $-y$ direction. The heat flux of the heater is assumed to be constant over its width.

the solution for the 2D heater, the 1D heater temperature is convolved with the rectangle function, defined as

$$\sqcap(x) = \begin{cases} \frac{1}{2b} & -b \leq x \leq b \\ 0 & \text{elsewhere.} \end{cases} \tag{2.32}$$

By using this source function, we assume that the heater is a uniform heat source over the interval $-b \leq x \leq b$. The factor of $1/2b$ is used to normalize the rectangle function; the purpose is to scale each 1D heater placed on the surface such that the sum transfers the same amount of heat to the substrate as before - the location of the heat source is "smeared out." To simplify notation, $\Delta\Theta_{AC}(x)$ is used to represent the oscillating temperature of the heater at $y = 0$. It is important to note that when mapping $\Delta\Theta_{AC}(r)$ to Cartesian coordinates that the function is symmetric about the y-axis, i.e. $\Delta\Theta_{AC}(x) = \Delta\Theta_{AC}(-x)$. The temperature at the surface caused by the 2D heater is then

$$\Delta T_{AC}(x) = \Delta\Theta_{AC}(x) * \sqcap(x), \tag{2.33}$$

where $*$ represents convolution. To evaluate this convolution, it is convenient to use the convolution theorem, which states that the Fourier transform $\mathcal{F}$ of a convolution in real

space is equivalent to multiplication in reciprocal space:

$$\mathcal{F}\{\Delta T_0 * \sqcap\} = \mathcal{F}\{\Delta T_0\} \cdot \mathcal{F}\{\sqcap\}. \tag{2.34}$$

After performing these operations, we take the inverse transform to find the real space temperature distribution.

The non-unitary transform of the $\sqcap$ function is easy to compute:

$$\begin{aligned} \mathcal{F}\{\sqcap\} &= \int_{-\infty}^{\infty} \sqcap(x) e^{-ikx} dx \\ &= \int_{-b}^{b} \frac{1}{2b} e^{-ikx} dx \\ &= \frac{\sin(kb)}{kb}. \end{aligned} \tag{2.35}$$

The transform of ΔT_0 is given by [7]

$$\mathcal{F}\{\Delta T_0\} = \frac{\langle P \rangle}{\pi l \kappa} \frac{\pi}{\sqrt{k^2 + q^2}}. \tag{2.36}$$

Now, the product of the transforms is

$$\mathcal{F}\{\Delta T_0\} \cdot \mathcal{F}\{\sqcap\} = \frac{\langle P \rangle}{\pi l \kappa} \frac{\pi \sin(kb)}{(kb)\sqrt{k^2 + q^2}}. \tag{2.37}$$

The inverse transform of this yields the convolution:

$$\begin{aligned} \Delta T_{AC}(x) &= \frac{1}{2\pi} \int_{-\infty}^{\infty} \mathcal{F}\{\Delta T_{1D}\} \cdot \mathcal{F}\{\sqcap\} e^{-ikx} dk \\ &= \frac{1}{2\pi} \int_{-\infty}^{\infty} \frac{\langle P \rangle}{\pi l \kappa} \frac{\pi \sin(kb)}{(kb)\sqrt{k^2 + q^2}} e^{-ikx} dk \\ &= \frac{2}{2\pi} \int_{0}^{\infty} \frac{\langle P \rangle}{\pi l \kappa} \frac{\pi \sin(kb)\cos(kx)}{(kb)\sqrt{k^2 + q^2}} dk \\ &= \frac{\langle P \rangle}{\pi l \kappa} \int_{0}^{\infty} \frac{\sin(kb)\cos(kx)}{(kb)\sqrt{k^2 + q^2}} dk \end{aligned} \tag{2.38}$$

Again, the even behavior of the integrand was used in this calculation. In the 3ω method, the average temperature of the heater is measured, which is calculated by integrating $\Delta T_{AC}(x)$ across the heater width and dividing by the width:

$$\begin{aligned}\Delta T_{AC} &= \frac{1}{2b}\int_{-b}^{b}\frac{\langle P\rangle}{\pi l\kappa}\int_{0}^{\infty}\frac{\sin(kb)\cos(kx)}{(kb)\sqrt{k^2+q^2}}dkdx \\ &= \frac{\langle P\rangle}{\pi l\kappa}\int_{0}^{\infty}\frac{\sin^2(kb)}{(kb)^2\sqrt{k^2+q^2}}dk.\end{aligned} \tag{2.39}$$

Thus, as a function of the current frequency, the temperature of the heater is

$$\Delta T_{AC}(f) = \frac{\langle P\rangle}{\pi l\kappa}\int_{0}^{\infty}\frac{\sin^2(kb)}{(kb)^2\sqrt{k^2+i4\pi f/D}}dk. \tag{2.40}$$

The in- and out-of-phase components of Equation 2.40 are plotted in Figure 2.5, along with the 1D heater model. Here we see that at low frequencies, the two models agree well, but the models are significantly different at high frequencies. This will be discussed in greater detail in Section 2.4.

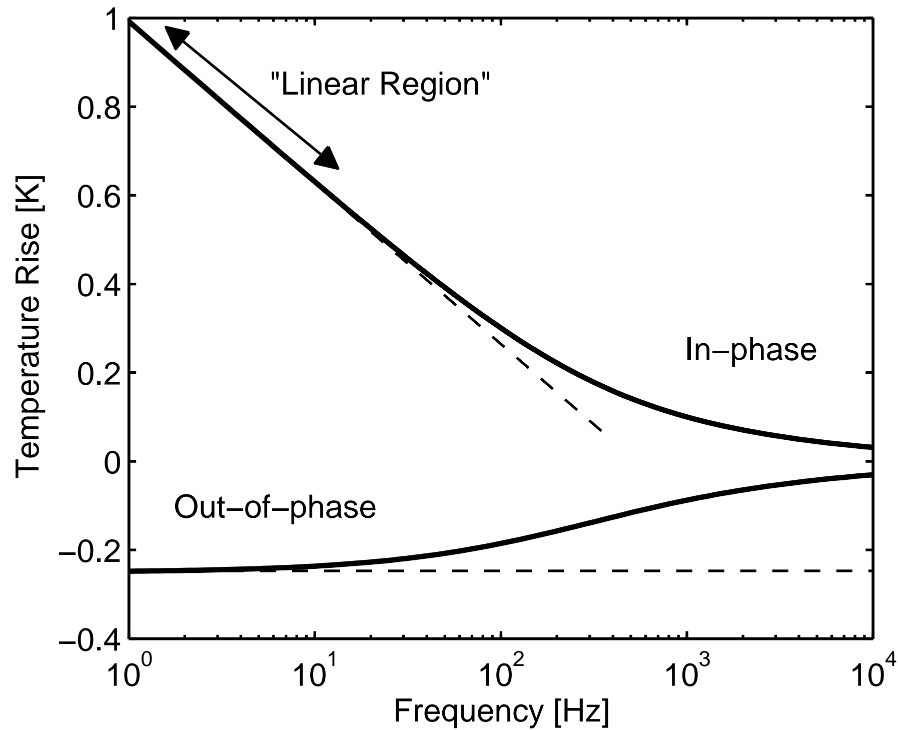

FIGURE 2.5: Modeled temperature *vs.* frequency curve for the 2D heater geometry. The dashed lines are the 1D approximation to the model. Parameters used are characteristic of amorphous glasses: $\langle P \rangle / l = 1$ W m^{-1}, $b = 10$ μm, $D = 1$ mm^2 s^{-1}.

As the heating frequency approaches zero, we see that the in-phase temperature increases and the out-of-phase temperature decreases to a constant (negative) value. In terms of amplitude and phase, the amplitude of the temperature increases and the phase shift becomes zero. As the heating frequency becomes large, the amplitude approaches zero and the phase shift approaches $-\pi/4$. It is useful to think of this behavior as being analogous to a simple RC electrical circuit; the heat flux (current) generated by the heater creates the temperature rise (voltage) across the substrate. The substrate has thermal mass (capacitance), so a steady state temperature is not reached instantaneously. The thermal mass causes the temperature to lag in time behind the heating. This lag becomes smaller at low frequencies because the thermal mass has time to "charge."

When comparing data from multiple measurements, it is often convenient to "normalize" temperature data to remove information about parameters such as the heating power and heater width. One way to do this is to convert all temperatures into thermal resistances. There is some ambiguity in the literature as to what quantity the term thermal resistance applies to. Here, thermal resistance is defined as

$$\Delta R_{th} = \frac{\Delta T}{Q}. \tag{2.41}$$

This thermal resistance describes the heat flux Q generated by applying a temperature gradient across a surface of area A. Typical units for $R_t h$ are $m^2 KMW^{-1}$. In terms of the 3ω measurements, $Q = \langle P \rangle / A$ and $A = 2bl$, the area of the heater in contact with sample. Thus,

$$\Delta R_{th} = \frac{2bl}{\langle P \rangle} \Delta T. \tag{2.42}$$

It is important to realize that this thermal resistance is characteristic of both material and heater properties. However, we will see in Section 2.5 that it is a useful quantity when performing measurements on thin films.

2.4. Parameters of the 2D Heater Model

There are a number of important parameters in the 2D heater model. κ and D are the measured material properties. The design of the heater geometry determines b and l. $\langle P \rangle$ is set, in principle, by the the current or voltage source used in the experiment, but also depends on the electrical resistance of the heater and therefore is dependent on b and l. In the measurement process, α, the temperature coefficient of resistance (TCR) of the heater is also important. This and the electrical resistivity of the heater are set by the material used to construct the heater. This section examines the effect of the parameters

κ, D, and b have on the temperature *vs.* frequency response of the 2D heater on substrate geometry.

In Section 2.2, we saw that the 1D heater produces a linear (on a logarithmic scale) in-phase temperature response and a constant out-of-phase temperature response. In Figure 2.5, we saw that at low frequency, the 2D solution does indeed converge to the 1D solution. This regime in which the two models agree is often referred to as the "linear region." The quantity $|1/q|$ is referred to as the thermal penetration depth and is characteristic of the distance that the thermal wave generated by the heater propagates over one cycle of heating [7]. Thus, at a set heating frequency, a substrate with a high thermal diffusivity has a higher thermal penetration depth than a substrate with a low thermal diffusivity. The temperature *vs.* frequency curve remains linear at higher frequencies for larger thermal diffusivity substrates. Physically, the linear region corresponds to the frequency range in which the thermal wave travels far enough away from the heater in one heating cycle that the 2D heater appears to be a line source (the temperature gradient is radially symmetric). When the current frequency is high enough, there is not enough time for the thermal wave to propagate away from the heater, making the finite width of the heater apparent. Thus, the 1D approximation is valid in the low current frequency regime where $|1/q| >> b$. In practice, $|1/q| > 10b$ is sufficient, meaning that materials such as silicon can have a linear region far into the tens of kilohertz range while the linear region for amorphous glasses is limited to tens of hertz. Figure 2.6 shows the thermal penetration depth *vs.* current frequency over a range of thermal diffusivities. In Figure 2.7, we see that the thermal diffusivity does not affect the slope of the linear region. Increasing the parameter D shifts the linear region up in temperature; this may seem unintuitive at first, as the diffusivity describes how quickly heat is conducted through a medium. However, as the diffusivity is inversely proportional to the heat capacity, it also describes how quickly a material will change temperature given a set heat flux; materials with a large

diffusivity respond quickly to the oscillating heat flux and therefore have a large increase in temperature over one heating cycle.

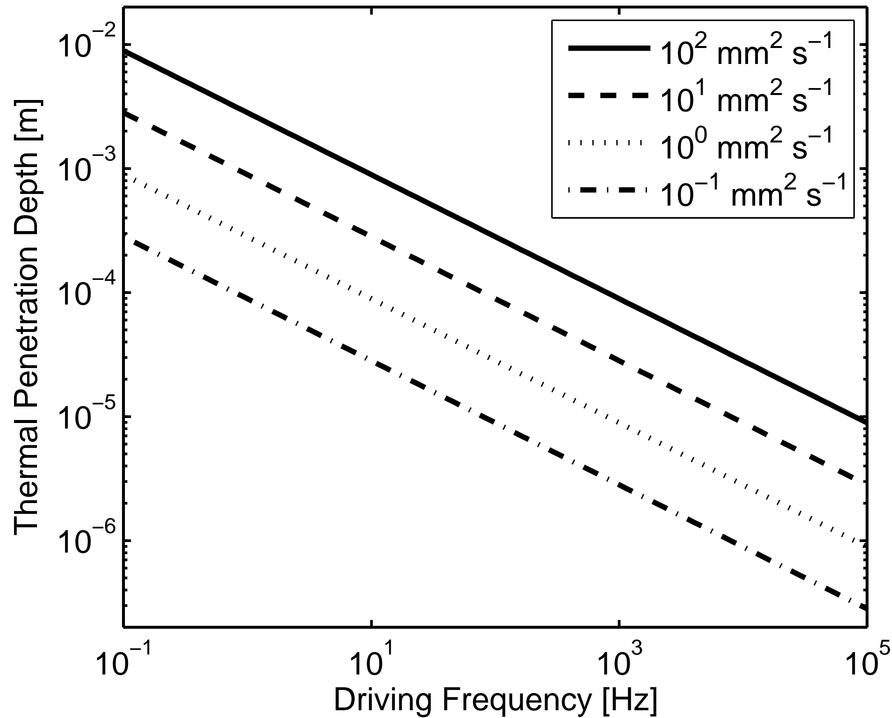

FIGURE 2.6: Thermal penetration depth *vs.* current frequency. Larger thermal diffusivities cause the thermal penetration depth to become larger, extending the linear region to higher frequencies.

In the 1D limit, we saw that Equation 2.30 can determine κ from the slope of the in-phase temperature *vs.* $\ln \omega$ curve. This slope is particularly useful as it is independent of D. Figures 2.7 and 2.8 confirm this approximation at low frequency. The thermal conductivity of the material directly changes the slope of the in-phase temperature curve at low frequency; the thermal diffusivity does not change this slope. For example, a measurement on a low thermal conductivity substrate results in a large (negative) slope. Decreasing the thermal conductivity of a substrate increases its thermal resistance, causing the temperature gradient across the substrate to increase for a given input heat flux.

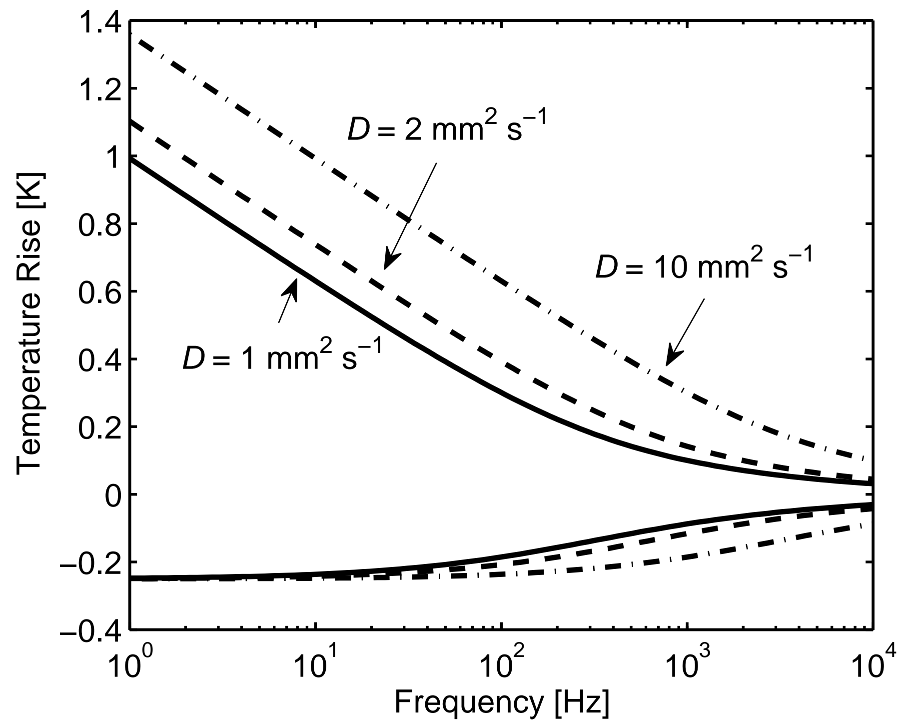

FIGURE 2.7: Effects of the substrate thermal diffusivity on the 2D heater model. $\langle P \rangle / l$ $= 1$ W m^{-1}, $b = 10$ μm, $\kappa = 1$ W m^{-1} K^{-1}.

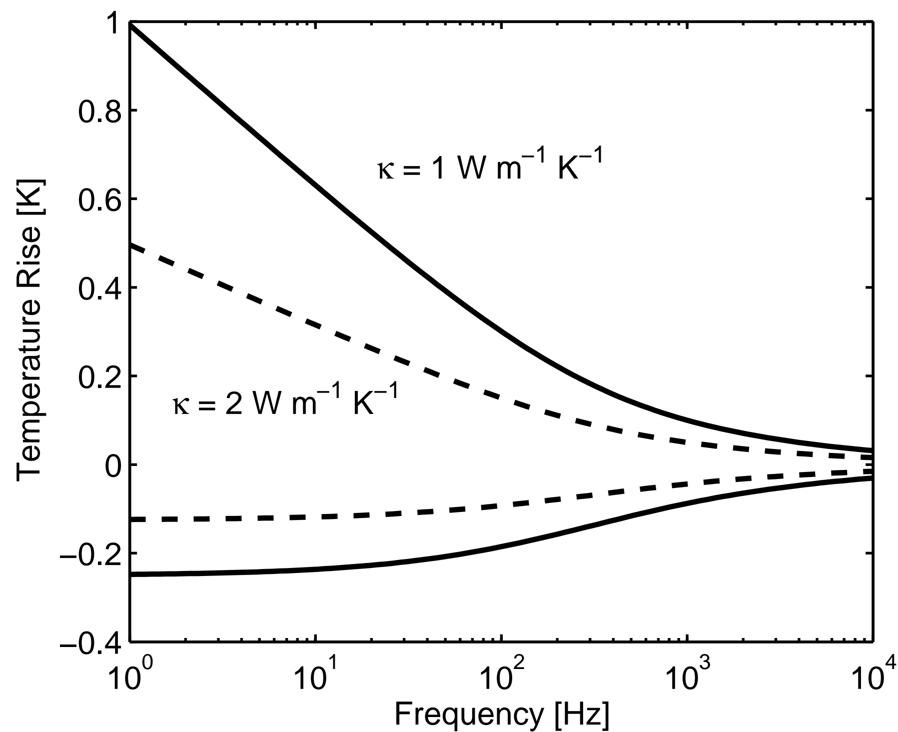

FIGURE 2.8: Effects of the substrate thermal conductivity on the 2D heater model. $\langle P \rangle / l$ $= 1$ W m^{-1}, $b = 10$ μm, $D = 1$ mm^2 s^{-1}.

As seen in Figure 2.9, the heater width plays a similar role in determining the broadness of the linear region. Using a wider heater means that the thermal penetration depth must be larger to exhibit 1D behavior. Therefore, decreasing the heater width extends the linear region to higher frequencies. As such, narrow heaters (less than 10 μm) are essential for making accurate thermal conductivity measurements using the 1D approximation on low diffusivity (and typically low conductivity) materials. However, if the thermal diffusivity is the property of interest, wider heaters can be used to limit the linear region and allow measurements of the high frequency regime, which is more sensitive to the diffusivity.

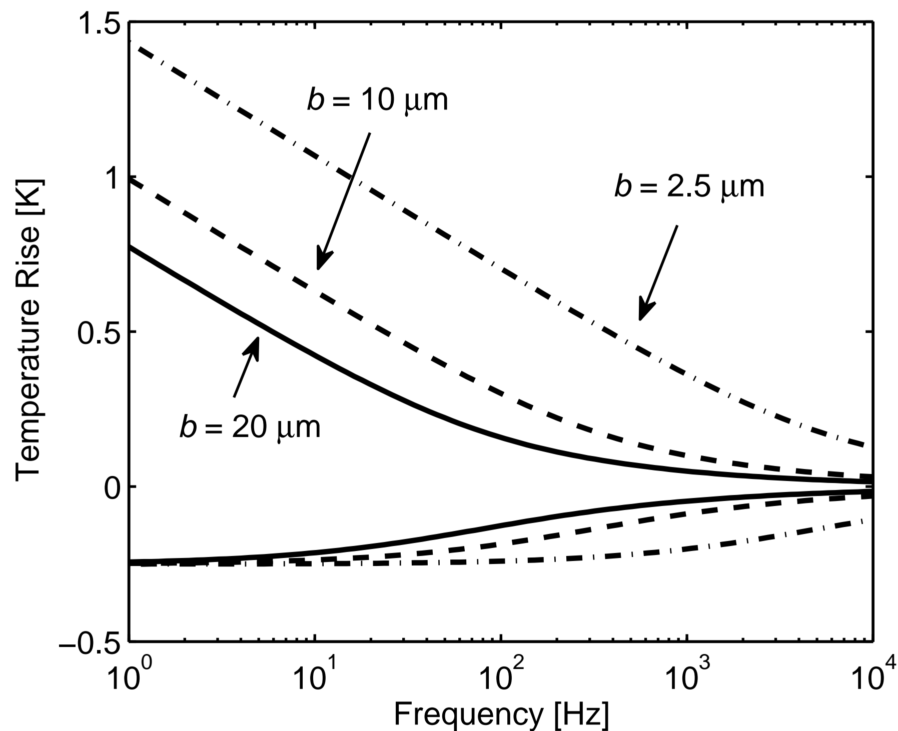

FIGURE 2.9: Effects of the heater width on the 2D heater model. $\langle P \rangle / l$ = 1 W m^{-1}, D = 1 mm^2 s^{-1}, κ = 1 W^2 m^{-1} K^{-1}.

2.5. The Thin Film Approximation

If a thin film of thickness d_f is inserted between the heater and substrate (see Figure 2.10), heat flow through the film is primarily cross-planar if the width of the heater is much greater than the thickness of the film ($2b >> d_f$). Under this assumption, the edge effects of the heater are small, so there is limited spreading in-plane spreading of the heat flow within the film. Figure 2.11 shows a substrate/film stack with two heaters, one with $2b << d_f$ and one with $2b >> d_f$. In this diagram, we see that heat flow from the narrow heater is primarily radial within the film, thus, in this regime, we expect behavior of the system similar to the 1D heater on a thick substrate. For the wider heater, it is clear that inside the film (near the heater), the pattern of heat flow suggests that the heater appears 2D; far away from the heater, where the thermal penetration depth is large compared to the film thickness, the pattern appears radial. This suggests that at low heating frequencies, the behavior of the film/substrate system is similar to the substrate only system. If we also assume that the thermal mass of the film is small (i.e., heating of the film is instantaneous compared to the heater frequency), we can treat the film as a thermal resistance and use Fourier's law to find the temperature gradient across the film.

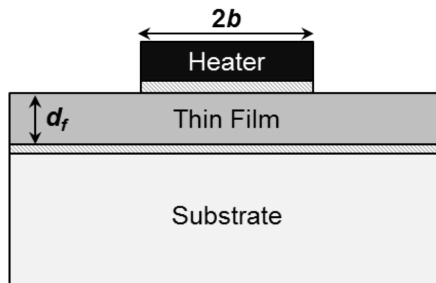

FIGURE 2.10: The thin film on substrate geometry. The shaded areas at the heater/film and film/substrate interfaces represent thermal interface resistance.

For a thin film in the x-z plane, the differential form of Fourier's Law reduces to

$$Q_y = -k_f \frac{d\Delta T_f}{dy}, \tag{2.43}$$

where Q_y is the heat flux through the film and κ_f is the film thermal conductivity. Assuming no spatial dependence on Q_y (the heater provides uniform heating) and κ_f, $q_f = \langle P \rangle / A$. $A = 2bl$ is the area of contact between the film and the heater. Solving Equation 2.43, the temperature gradient across the film is

$$\Delta T_f = \int_0^{d_f} \frac{\langle P \rangle}{2bl\kappa_f} dy = \frac{\langle P \rangle d_f}{2bl\kappa_f}. \tag{2.44}$$

At low frequency ($|1/q| >> d_f$), the film causes a frequency-independent increase to the temperature of the heater. There is no change to the out-of-phase temperature as there is no phase-shift associated with the film. This is due to the assumption that the film has significantly low thermal mass that heating of the film takes place instantaneously. As seen in Figure 2.12, thicker films, having a larger thermal resistance, cause a larger temperature increase. Similarly, films with lower thermal conductivity also cause a larger temperature increase. In the case of a thin film, the thermal resistance, given by Equation 2.42 is

$$\Delta R_{th,f} = \frac{d_f}{\kappa_f}. \tag{2.45}$$

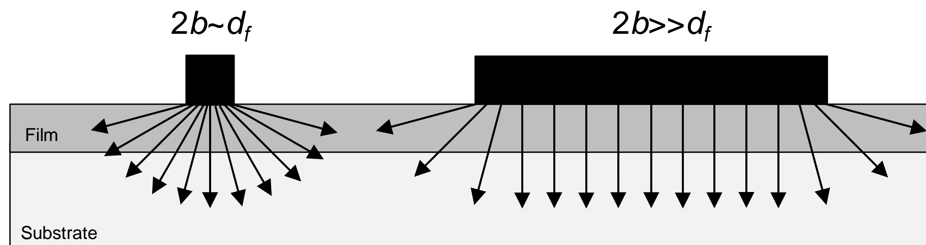

FIGURE 2.11: Heat flow through a thin film using heaters with $2b$ d_f and $2b >> d_f$.

If the samples consists of stack of multiple films, the thermal resistances add. Thus, it is easy to calculate the temperature rise caused by multiple films at low frequencies.

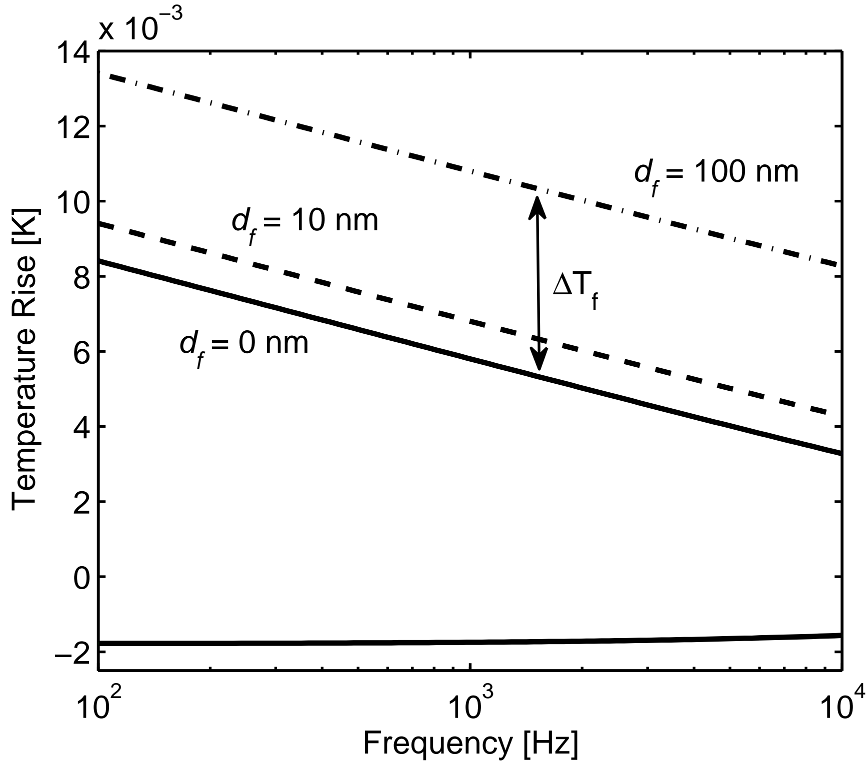

FIGURE 2.12: Effects of adding a thin film to the 2D heater model. In the linear region, the film adds a frequency independent increase to the in-phase temperature.

In the 3ω geometry, it is critical to realize that there is thermal resistance at each material interface. This includes the substrate/film and the film/substrate interfaces, shown in Figure 2.10. These thermal interfaces are inherently difficult to characterize, because they depend strongly on the mechanical contact of the materials at the interface and material properties. In the linear region, these thermal interfaces behave like thin films and have a definable thermal resistance that also causes a frequency independent increase in the temperature. For measurements of the substrate thermal conductivity using the slope of the linear region, these interfaces are not a major concern. However, they complicate measurements on thin films greatly as the film thermal conductivity cannot

be determined without prior knowledge of the interface resistances, which is typically unknown and difficult to measure. The linear behavior of the film thermal resistance with the film thickness suggests a way to work around this problem. By taking measurements on multiple samples of the same substrate and film material and varying only the film thickness of each sample, an experimental relation between $\Delta R_{th,f}$ and d_f can be established. This relationship is linear with slope $1/\kappa_f$. The sum of all interface resistances, ΔR_i, is seen as an offset at the zero film thickness intercept.

2.6. Measuring the Temperature: The 3ω Voltage

Increasing the temperature of a metal also increases its resistance. Over a small temperature range, the relationship is linear. The proportionality constant is known as the temperature coefficient of resistance α. We can use this property of metals to experimentally measure the temperature of the 3ω heater. For small temperature variations, the resistance of the heater is

$$R(t) = R_0\big(1 + \alpha\Delta T_{DC} + \alpha\Delta T_{AC}\cos(2\omega t + \phi(\omega))\big), \tag{2.46}$$

where R_0 is the resistance of the heater at ambient temperature and ΔT_{DC} and ΔT_{AC} are the constant and oscillating increases of the temperature of the heater above ambient. The frequency dependent phase angle $\phi(\omega)$ is introduced to take into account any time delay between the driving current and the thermal response of the heater. Measuring the

voltage across the heater gives

$$\begin{aligned} V(t) &= I(t)R(t) \\ &= I_0R_0\cos(\omega t)\Big(1+\alpha\Delta T_{DC}+\alpha\Delta T_{AC}\cos(2\omega t+\phi)\Big) \\ &= I_0R_0\Big((1+\alpha\Delta T_{DC})\cos(\omega t)+\frac{1}{2}\alpha\Delta T_{AC}\cos(\omega t+\phi) \\ &\qquad +\frac{1}{2}\alpha\Delta T_{AC}\cos(3\omega t+\phi)\Big). \end{aligned} \tag{2.47}$$

The voltage across the heater is a superposition of three signals; one oscillates at a frequency of ω and is in phase with the driving current; the second also has frequency ω but is phase shifted by the factor ϕ which is a function of ω; the last signal has frequency 3ω and is phase shifted by the same factor. In practice, both α and the temperature rise of the heater are small, so the "new" 1ω and 3ω terms are typically 60-80 dB smaller than the Ohmic response. The voltage component with frequency 3ω is known as the 3ω voltage:

$$V_{3\omega}(t) = \frac{1}{2}I_0R_0\alpha\Delta T_{AC}\cos(3\omega t+\phi). \tag{2.48}$$

If the 3ω component of the voltage is measured, the magnitude of the temperature oscillations is determined by the formula

$$\Delta T_{AC} = \frac{2V_{3\omega}}{\alpha I_0 R_0}. \tag{2.49}$$

It is usually easier to measure the $V_{1\omega}$, the magnitude of the 1ω component of the voltage across the heater. Since $V_{1\omega} \approx I_0R_0$, Equation 2.49 is rewritten as

$$\Delta T_{AC} = \frac{2V_{3\omega}}{\alpha V_{1\omega}}. \tag{2.50}$$

For this experiment, both the magnitude and relative phase of the temperature oscillations are important. As shown previously, it is convenient to describe the temperature rise in

terms of the in- and out-of-phase components $\Delta T_{AC,x}$ and $\Delta T_{AC,y}$:

$$\Delta T_{AC,x} = \frac{2V_{3\omega}}{\alpha V_{1\omega}} \cos(\phi) = \frac{2V_{3\omega,x}}{\alpha V_{1\omega}} \tag{2.51}$$

$$\Delta T_{AC,y} = \frac{2V_{3\omega}}{\alpha V_{1\omega}} \sin(\phi) = \frac{2V_{3\omega,y}}{\alpha V_{1\omega}}. \tag{2.52}$$

These in- and out-of-phase temperature components are the same components described in earlier in this chapter. To measure the 3ω voltage in practice, it needs to be isolated from the 1ω voltage. Methods of doing this are discussed in detail in Chapter 3.

3. EXPERIMENTAL APPARATUS

3.1. Heater Design

As seen in Chapter 2, the geometry of the 3ω heater is critical to the measurement. To use the 2D heater model, the heater must be extremely rectangular; jagged edges, inconsistent width of thickness, and other anomalies limit the accuracy of the measurement system. In addition, there are small effects not taken into account in the 2D model that place constraints on the design of the heater. These include electrical and thermal edge effects and thermal diffusion within the heater.

Figure 3.1 shows the two heater types commonly used with the 3ω method. The first heater type uses two large contact pads at either end of the heater. Both current and voltage probes are placed on this contact pad. The two-pad heater is useful because of its simple design and ease of patterning, but it does have some drawbacks. For example, if the contact pads are large, there may be a significant voltage drop across the pad, resulting in inaccurate voltage measurements. However, the main concern is measurement inaccuracy due to a non constant temperature profile of the heater. As shown by Zong *et al.* [12], the temperature profile of the heater is not constant, as is assumed in the model. It is also dependent on the frequency of the driving current.

Figure 3.2 shows a simulation of the temperature rise along the length of a two contact pad heater using a finite element method. The contact pads have a large thermal mass compared to the heater itself; therefore, they act as a heat sinks, allowing heat generated within the heater to flow outward. The result is a larger temperature rise in the center of the heater than at the edges. The effect is more pronounced at low frequencies, when the temperature gradient is larger and heat has more time to propagate down the heater over the course of one oscillation. To compensate for this phenomenon, heaters

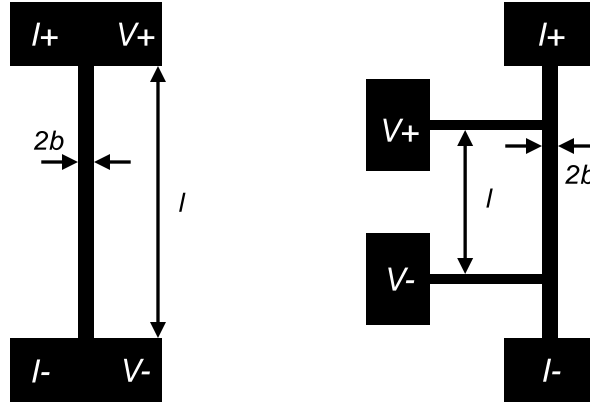

FIGURE 3.1: Two and four contact pads designs of the 3ω heater.

with four contact pads are used in the geometry shown in Figure 3.1. The current pads are placed at the ends of the heater and leads connect the voltage pads directly to the heater. This allows the voltage measurement to be made only over the range where the temperature profile is approximately constant. Simulations show that there is a small drop in temperature where the voltage leads connect to the heater, but this effect is significantly smaller than the effect seen at the heater ends. The four-pad heater design also has the benefit of eliminating problems with voltage drops across contact pads.

The material used for the heater is also crucial. Typically, a high resistivity metal with a large TCR is chosen to maximize the size of the 3ω signal. Metals that fit into this category are aluminum, copper, silver, gold, nickel, and platinum. Figure 3.3 gives resistivity and TCR values for several metals. In practice, these values are not accurate as both the resistivity and temperature coefficient of the heater depend heavily on the heater deposition process; variations of 50% from literature values are not atypical, especially for materials that easily oxidize (such as aluminum). Thus, it is extremely important to measure the TCR for each heater.

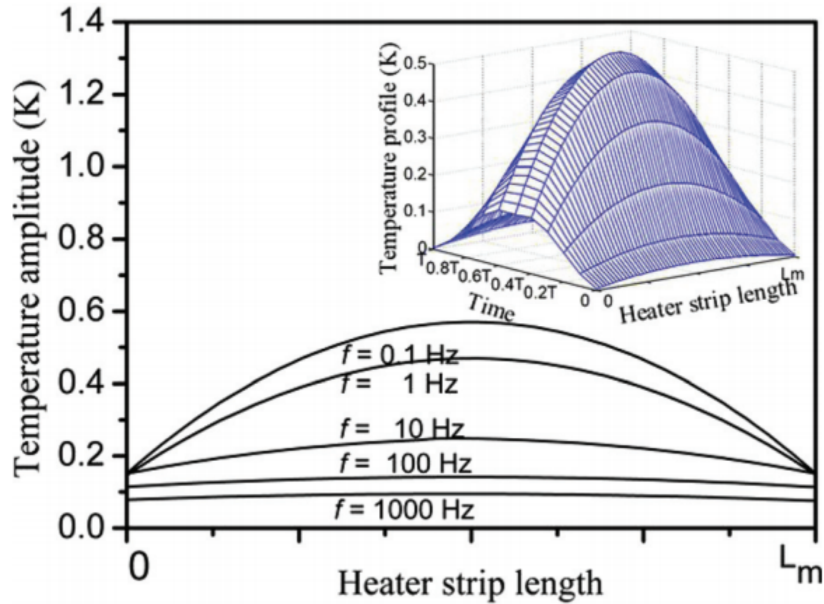

FIGURE 3.2: Simulated temperature rise along the length of a heater with two contact pads. At low heating frequencies, the temperature profile varies greatly across the heater length. As the frequency increases, this profile becomes uniform. From [12].

For conventional voltage-driven setups, heaters with a total resistance of 50 Ω work well, although we have successfully used heaters ranging from 10-100 Ω. The deposition process used for the heaters is also important to consider when choosing a material; for instance, most metals will not adhere to the sample with thermal evaporation. In some cases (such as with aluminum), the substrate can be heated during deposition to substantially improve adhesion, reducing thermal resistance at the interface (this is extremely important for thin film measurements). In other cases (gold, silver, and platinum), a thin adhesion layer (typically titanium or chromium) must be placed between the sample and the heater material to achieve even mechanical adhesion.

For typical sample sizes (5 cm^2), multiple heaters can be deposited on each sample. This is advantageous for many reasons. For instance, if a heater is damaged during or after the production process, the sample may still be usable. Testing the sample with multiple heaters allows a check on the accuracy of the measurements and to determine

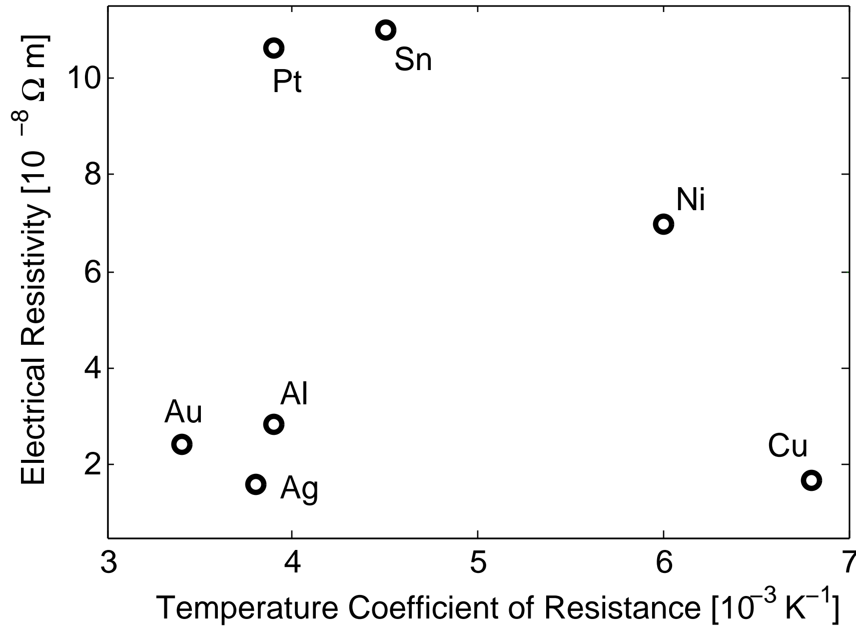

FIGURE 3.3: Electrical resistivity *vs.* temperature coefficient of resistance for several metals. Data are for measurements made at room temperature. Data from [17].

whether the heater width has any effect on the calculated thermal conductivity.

We have found that a simple lift-off process allows us to create usable 1 mm long heaters with widths as small as 5 μm. For thin film measurements, 20 μm wide heaters are typically used as they are sufficiently wide to make the condition that $b >> d_f$ true and they are sufficiently small that the heater resistance is reasonably large ($> 10\Omega$) for aluminum heaters of thickness 180 nm.

The following lithography process (see Figure 3.4) is used to pattern the heaters:

1. Samples are first cleaned with 18 MΩ cm deionized (DI) water, acetone, methanol, isopropynol, DI water, each in an ultrasonic bath for 15 minutes.
2. Samples are then blown dry with nitrogen and baked at 115 °C on a hot plate for 2 minutes.
3. Photoresist primer, Microchem MCC 80/20, is spun onto sample at 3000 rpm for 30

seconds. During this process, interference fringes from the primer are often observed. The changing color indicates that the thickness of the primer is changing. By the end of the spinning, the color should stop changing. The primer allows for good adhesion between the sample and the photoresist.

4. The sample is "soft baked" at 85 °C for 2 minutes.

5. The photoresist, Microposit S1813, is spun onto the sample at 3000 rpm for 30 seconds. Again, interference fringes can be seen during this process. The photoresist should be visibly uniform over the surface of the sample. Any streaks in the resist are likely caused by particles on the sample surface.

6. The sample is again soft baked at 85 °C for 2 minutes.

7. The photoresist is exposed to UV light through a chrome-quartz mask. This mask is previously cleaned to remove dust and other debris prior to putting it in the contact mask aligner. Depending on the contact aligner and lamp power, exposure times vary. For the ECE418 contact aligner at OSU, a six second exposure with a lamp power of 350 W works well for thin films on silicon substrates.

8. The resist is developed in Microposit 351 for 15 seconds, followed by an immediate rinse for one minute in DI water.

9. The sample is "hard baked" at 115 °C for 2 minutes.

10. Samples are placed in an ultrasonic bath for 15 minutes in 18 MΩ cm DI water to remove photoresist residue.

11. An aluminum film is deposited by thermal evaporation. Base pressure for the deposition is less than 5 uTorr. Substrates are heated to approximately 150 °C during the deposition to assure good adhesion of the metal. If a series of samples is being made, heaters are deposited on all samples simultaneously to achieve consistent TCR and thermal interface results. If other deposition processes are used (such as e-beam or

sputtering), substrate heating may not be required to achieve proper adhesion.

12. Samples are cooled to room temperature before removing from vacuum to avoid oxidation of the metal film.

13. Samples are sonicated in acetone to remove the unwanted resist layer. This takes about 5-10 minutes.

14. The acetone residue is removed with isopropynol and samples are blown dry with nitrogen.

We have also made aluminum heaters using electron beam evaporation. If e-beam is used instead of thermal evaporation, substrate heating during the deposition is not required to achieve good adhesion of the aluminum film to the sample. This is likely due to the higher particle kinetic energy associated with e-beam.

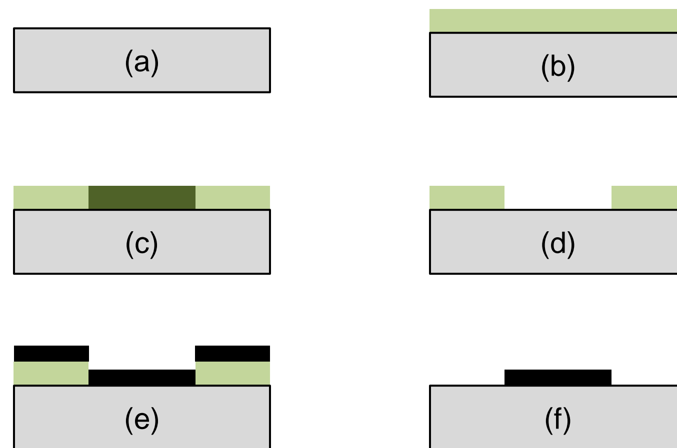

FIGURE 3.4: Diagrams of the lift-off photolithography process.(a) The process starts with a bare, cleaned sample. (b) The sample is coated with a layer of photoresist primer and photoresist (light green). (c) Selected areas of the resist are patterned by exposure to UV light (dark green). (d) After exposure, the sample is placed in a developer solution, removing the exposed resist. (e) A thin metal film (black) is deposited on the sample. (f) The sample is placed in a solvent that selectively removes the resist, leaving only the patterned metal film behind.

Figure 3.5 shows microscope images of a 20-μm and a 5-μm wide aluminum heater made with our lithography process. These heaters have consistent width along their entire length. The edges of the heaters are relatively smooth, with the largest of variations being less than 1-μm. There is no evidence of significant shadowing at the edges of the heater.

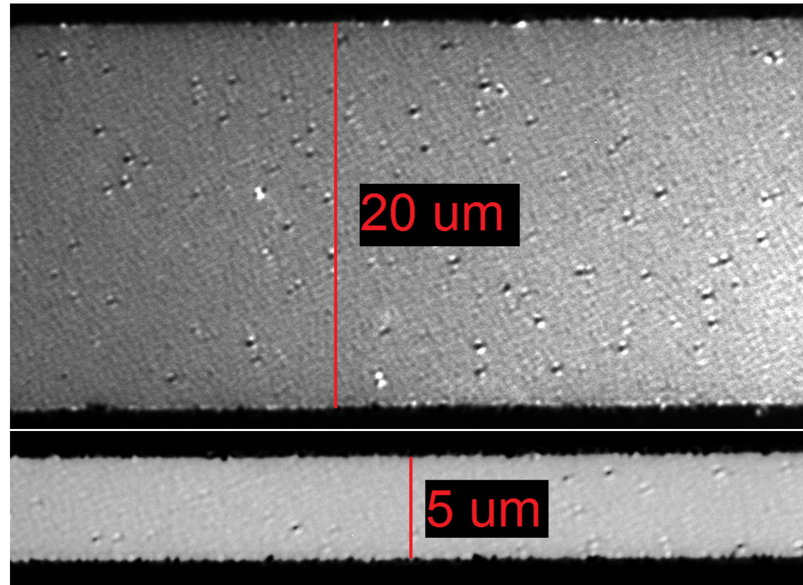

FIGURE 3.5: Microscope images of a 20-μm and a 5-μm wide heater produced by the photolithography process.

3.2. Measurement System

The goal of the 3ω measurement system is to apply a sinusoidal voltage at frequency ω across a sample heater and measure the 3ω voltage response over a wide range of frequencies. In brief, a digital function generator creates the applied 1ω voltage. A custom built circuit measures the total voltage across the sample and subtracts the large 1ω voltage leaving mostly the important 3ω voltage. A lock-in amplifier (referenced to the function generator) further isolates the 3ω voltage and performs precise measurements of its amplitude and phase. A digital oscilloscope measures the 1ω voltage across the sample

and the 1ω current through the sample. A heated substrate holder and thermocouple allow the temperature of the sample to be altered for TCR measurements. A LabVIEW program automates the process, allowing large datasets to be taken automatically.

3.2.1 Subtraction Circuit

A custom built subtraction circuit is used to isolate the third harmonic from the voltage across the heater and make simultaneous measurements of the current and voltage through the heater. Figure 3.6 shows a functional schematic of the subtraction circuit.

The 1ω current from the function generator is applied to the positive current contact pad (I_+ on Figure 3.1) on the sample heater. A is a unity gain instrumentation amplifier (Texas Instruments INA128P). The positive and negative inputs of this amplifier are connected to corresponding voltage contact pads (V_+ and V_-) on the heater. The output of A is simply $V_+ - V_-$.

I_- is connected to a tunable resistor network. This network consists of thermally stable, thick film resistors (Ohmite TCH35P series with TCRs less than 100 ppm°C [18] that can be adjusted to match the resistance of the heater to within 1Ω). These resistors are heat sunk to a large aluminum plate to further improve their thermal stability. The resistance of the network is tuned by placing multiple resistors in series. A rheostat is not used in order to reduce inductance and prevent any high-frequency problems resulting from stray reactance. B measures the voltage across the resistor network. If the resistance of the network is the same as heater, the output of B is the same as the output of A, without the voltage terms related to the thermal oscillations of the heater. The gain of B is close to unity, but can be adjusted to further match the amplitude of 1ω part of the amplifier outputs.

C is used to subtract the output of B from A. This amplifier is either the built in differential input of the lock-in or an external INA128P. If the resistance of the resistor network is matched to that of the heater and the gain of B is properly tuned, the output

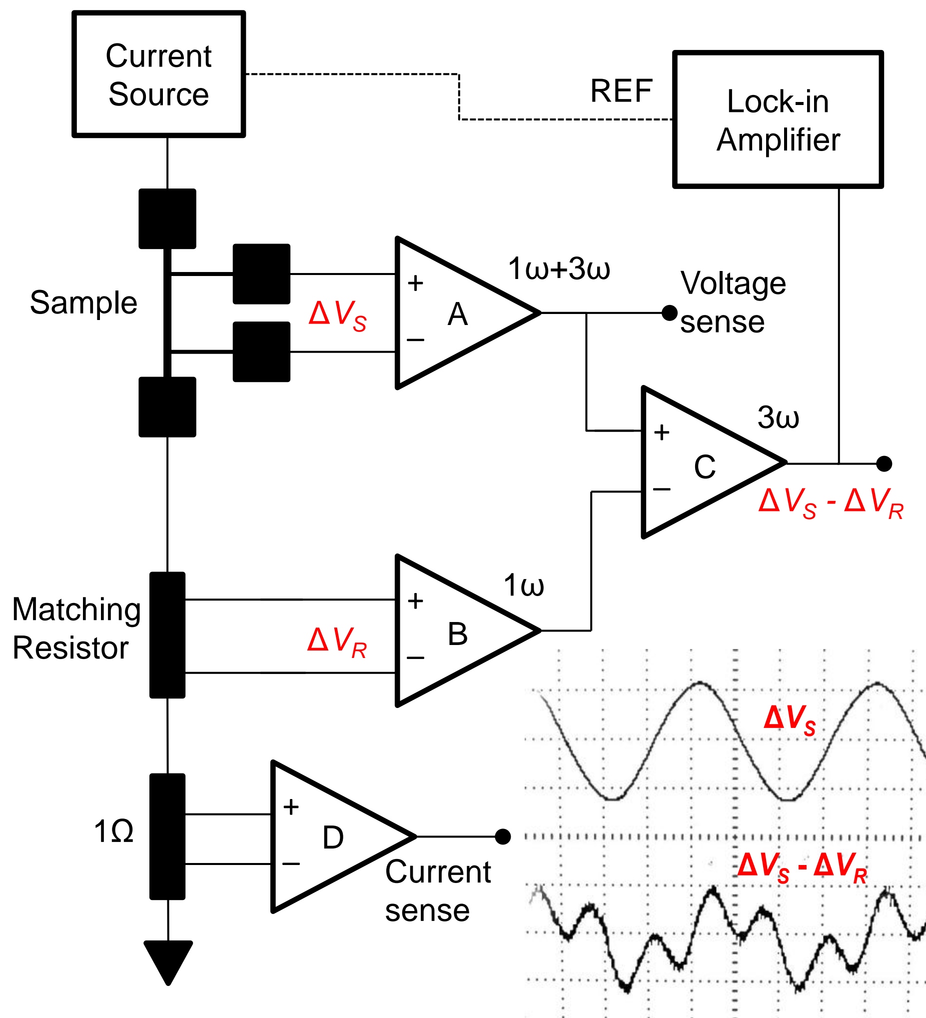

FIGURE 3.6: Schematic of the subtraction circuit. Inset shows the output of amplifiers A (top signal, heater voltage before subtraction) and C (bottom signal, heater voltage after subtraction). The scale of the bottom signal is about 1/1000 of the top signal.

of C is primarily the 3ω component of the voltage across the heater. In addition to rejecting the large 1ω voltage, other harmonic distortion created by the function generator is attenuated, resulting in increased precision of the 3ω voltage and allowing a voltage generator to be used in place of a current generator [19].

D measures the voltage across a thermally stable 1 Ω resistor connected in series with the heater and resistor network. If the resistance is precisely known, this voltage measurement provides a measurement of the current through the heater via Ohm's law. The calibration consists of connecting an ammeter in series with the resistor and tuning the gain of D until a 1 V to 1 A voltage to current ratio is achieved.

RMS voltage measurements of the outputs of A and D are measured by an oscilloscope (Agilent DSO-X 2002A) to determine the RMS voltage across and current through the heater. These values determine the RMS power dissipated by the heater and the resistance of the heater. It is important to note that these resistance measurements are 4-point measurements, so the lead and contact resistances are removed.

One limitation to the frequency range of the measurement system is bandwidth of the instrumentation amplifiers. The transfer function of an INA128P amplifier is shown in Figure 3.7. For this measurement, the lock-in was used as both the voltage source and measurement device, so its own frequency limitations are included in this figure. We see that the system performs well at low frequencies but begins to exhibit problems at frequencies above 10 kHz. From this, we judge the upper limit to the system to be 10 kHz, realizing that other factors, such as bad electrical contacts to samples and stray reactance within the rest of the subtraction circuit or samples may further limit this range. In addition to the frequency range of the instrumentation amplifiers, the lock-in is also limited in frequency to 102.4 kHz [20] (for the 3ω voltage), which corresponds to a maximum current frequency of approximately 34 kHz.

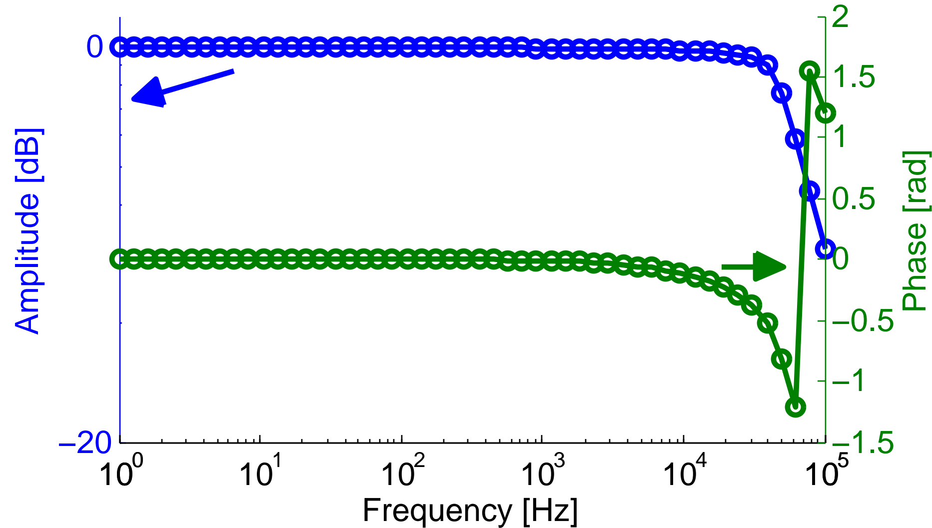

FIGURE 3.7: Transfer function of an INA128P amplifier. The amplitude begins to roll off around 10 kHz. Changes in the relative phase are even more apparent.

3.2.2 Lock-in Amplifier and Automation

Lock-in amplifiers are used to isolate signals by "locking onto" a particular frequency and rejecting all others. This method allows voltages with a very low signal to noise ratio to be measured. A lock-in amplifier requires a reference signal to determine the frequency and relative phase of voltage to be measured. Modern digital lock-ins can also measure to higher harmonics of the reference signal. A detailed introduction to lock-in amplifiers by Stanford Research Systems is found in [21].

We use the SRS SR850 digital lock-in amplifier to measure the 3ω voltage. The lock-in takes the output of the subtraction circuit and further attenuates all signals not at 3ω. The SR850 also functions as a function generator by supplying a connection to its internal oscillator. In this case, the lock-in does not require an external reference signal as all referencing is done internally. The lock-in is also the preferred voltage source in the

3ω measurements due to its low harmonic distortion (-80 dBc) and high phase resolution (0.01%) [20].

An Agilent Technologies DSO-X-2002A digital oscilloscope monitors the outputs of instrumentation amplifiers A and D. The oscilloscope continuously measures and displays the rms voltage output of these amplifiers. This effectively measures the 1ω voltage across and 1ω current through the heater. Combined, these values give the average power generated by the heater.

Before the measurement is made, the measurement system must be configured appropriately. The following procedure assumes that the lock-in is used as the current source for the measurement:

1. The sample is properly connected to the measurement circuit.
2. In the "REF PHASE" menu on the lock-in amplifier, "Sine Output" is set to the input voltage for the measurement. This is typically 5 V.
3. In the "INPUT FILTERS" menu, "Coupling" is set to "DC." AC coupling causes significant phase errors in the measurement below 100 Hz.
4. The resistance of the matching resistor bank is set to the maximum value below the sample resistance. The gain of amplifier B is then adjusted to cancel out the 1ω voltage all the way.
5. In the "REF PHASE" menu, "Harmonic" is set to "1."
6. In the "INPUT FILTERS" menu, "Source" is set to "A."
7. In the "GAIN TC" menu, "Sensitivity" is set to its minimum value (maximum full scale voltage).
8. In the "GAIN TC" menu, the "Time Constant" is set to an appropriate value. For measurements above 100 Hz, 3 s is sufficient. For lower frequency measurements, larger time constants must be used to achieve proper stabilization.

9. The phase of the internal reference is "zeroed." This is accomplished by pressing the "AUTO PHASE" button on the lock-in until the out-of-phase voltage (Y) is zero. This means that the phase of the driving voltage is defined as zero phase.

10. Because we really want to lock-on to the 3ω signal in time rather than in phase (a phase shift for a 1ω signal is not the same shift in time as for a 3ω signal), we must adjust the reference phase from its autophased value. In the "REF PHASE" menu, "Ref. Phase" is set to three times its displayed value. Typically, this value is small unless and external current source is used.

11. "Harmonic" is set to "3." The lock-in is now properly locked-on to the 3ω signal.

12. "Source" is set to "$A - B$" if amplifier C is the differential input of the lock-in. Otherwise, this is left on "A."

13. "Sensitivity" is set to its the maximum value such that the full scale voltage is still greater than the maximum voltage that will be measured.

14. In the "GAIN TC" menu, "Reserve" is set to an appropriate value. Typically the "MAX" setting works well.

15. In the "GAIN TC" menu, " Filter" is set to "24 dB/oct.". The synchronous filter does not seem to affect the measurement.

16. The system is now ready to take automated measurements.

A LabVIEW program was created to interface directly to the lock-in and oscilloscope. This program accepts several inputs from the user, including the measurement frequency range and the number of data points to take. The program sets the frequency of the lock-in generated voltage and records the in- and out-of-phase voltages when the signal has stabilized. For each frequency point, the oscilloscope acquires for the voltage outputs of amplifiers A and D.

A customized stabilization routine ensures that the lock-in voltage signals have

indeed settled before data is recorded and the program moves to the next data point. This stabilization routine monitors the voltage amplitude over time (typically at a rate of 10 Hz) and takes a numerical time derivative of this amplitude. The values of this derivative are stored in a continuously updating buffer. This buffer holds a set number of data points (typically 100). When all of the values in the buffer are below a user set threshold, the signal is considered stabilized and the program moves to the next data point. The amplitude and derivative are both displayed in graph form so the user can also monitor the stabilization and make any necessary adjustments to the input parameters.

Figure 3.8 shows a functional schematic of the automation software. The program accepts a list of inputs from the user, including the frequency range to sweep over, the number of data points to take, the direction of the frequency sweep (up or down in frequency), and whether the data points are taken with equal spacing on a linear or logarithmic scale. The stabilization settings are also input. Settings specific to the lock-in amplifier (time constants, phase settings, etc.) are set directly on the lock-in or through a separate initialization program; these settings typically do not change from measurement to measurement.

Once the user sets all inputs, the program sets the lock-in frequency to the first frequency to measure. The stabilization sub-program queries the stabilization settings and waits for the voltages to stabilize. The program then 3ω voltage data from the lock-in and the rms voltage and current data from the oscilloscope (for the 1ω voltage and current measurements). The data is stored and the graphs on the program interface are updated. If there are still more frequency data points to take, the program repeats the process in a loop; otherwise, the program ends.

3.2.3 Substrate Heating

The substrate heater, seen in Figure 3.9 consists of a polished copper block with either one or two 1/4 W cartridge heaters embedded in the block. A thermocouple can be

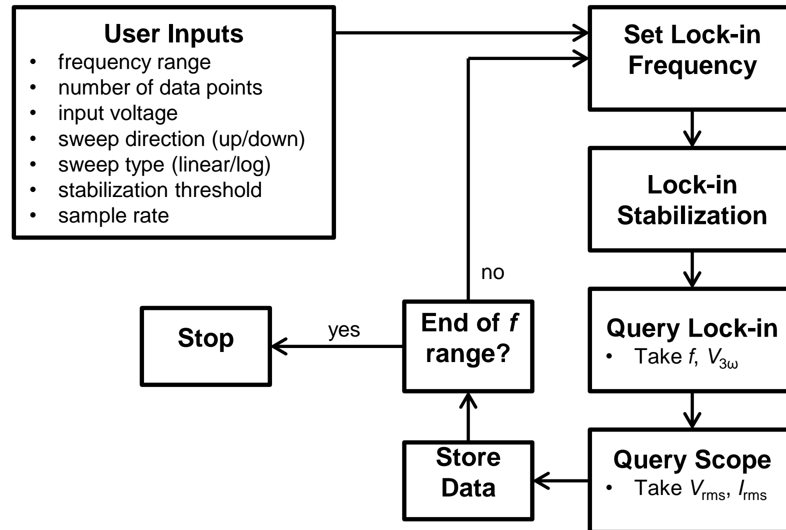

FIGURE 3.8: Functional schematic of the LabVIEW automation program.

mounted internally between the heaters. The temperature of the block can be controlled either with a standard PID controller or by simply connecting the heaters to a DC or AC voltage source (such as an autotransformer). The latter method is typically used for TCR measurements as a slow increase in temperature of only a few degrees Celsius is required.

For TCR measurements, an additional thermocouple is connected to the surface of the substrate, near the heater. This allows for a more accurate temperature measurement then the internal thermocouple can provide, due to the thermal resistance of the sample substrate and various interface resistances. Various methods of attaching this thermocouple have been tested. Mechanical contact is the simplest, but often creates a connection with a large thermal resistance, resulting in an unreliable measurement. Epoxies lower the thermal resistance of the connection, but often have long drying times make removal of the thermocouple from the sample difficult. With practice, clear nail polish can be used to make reliable, small footprint connections. In addition, nail polish residue is easily removed from the thermocouple and sample with a Q-tip dipped in acetone.

3.2.4 Electrical Contact to Heater

Low resistance, Ohmic electrical contacts to the heater are important to improve signal stability and reduce distortion. Several methods of contact have been tested. These methods fit into three categories: mechanical contacts, soldered contacts, and conductive epoxies. Mechanical contacts use force to press a conductive probe against the contact pad. Spring-loaded pins (also known as pogo pins) work best for this. The pins can be mounted in a movable frame, allowing samples to be connected quickly and easily. The applied force on each pin can be controlled, allowing for a repeatable contact profile over many samples. Pogo pins with a flat probe tip were found to have to best results; their large surface area allows for low contact resistance. The flat probes also prevent damage to the contact pads and sample. Sharp probes tend to puncture the contact pads, resulting in bad electrical contact and damage to the sample. If the sample has a conducting film or substrate, this would result in a unusable sample. A small amount of silver paint or conductive epoxy applied to the probe tip can improve the contact resistance or fix damaged pads.

In principle, a well soldered contact will have a lower contact resistance and more linear IV curve than the best mechanical connections. In practice, high quality soldered connections are difficult to make for this geometry. Due to the small surface area of the contact pads, small solder joints must be used, which requires both time and skill. The high temperature associated with soldering can easily damage the heaters by causing significant oxidation of the aluminum surface. Chemical reactivity of the solders with the aluminum is also a consideration. The necessary mechanical contact of the soldering tip to the contact pad can damage both the pad and the underlying film or substrate. Use of an air-soldering iron can eliminate this type of damage.

Conductive epoxies can be used to create low resistance electrical contacts without damaging the contact pads or sample. However, long drying times for epoxies (hours to

days) plague this technique. Contacts made by this method are also single use, due to the difficultly in removing epoxy from the sample once it has been applied.

3.2.5 Sample Holder

We constructed a sample holder that combines the both substrate heater and electrical probes into one apparatus. As seen in Figure 3.9, the substrate heater is placed inside an embossed plate. The heater is easily removable so the copper surface can be cleaned and polished to ensure that there is minimal thermal resistance between the substrate and the copper block. The pogo pins consist of a socket and a pin; the socket, which contains the spring and external electrical connections, is fixed in place. The pin slides into the socket and is removable, allowing for the replacement of aged pins. This pogo pin assembly is mounted to another plate, which slides vertically on two linear dowels. Each of the pogo pins are attached to electrical leads that connect directly to the subtraction circuit.

When making contact to the sample, the controlled vertical motion of the pogo pins prevents scrub and scratch damage to the sample's contact pads. The amount of pressure applied by the pins is dependent on the weight of the upper plate; additional mass can be placed on the plate to increase this pressure, allowing for a better electrical contact. However, too much pressure can puncture the contact pads and damage the sample surface. If there is a conductive layer within the sample, this damage can cause an electrical short between the pogo pins and the conductive layer, potentially leading to error in measurements of current through the heater and by creating distortion and instability in the measured signal.

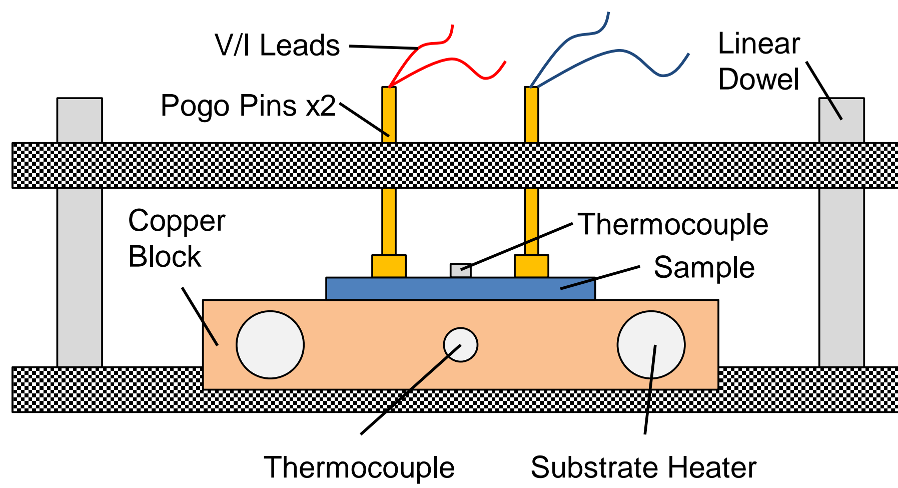

FIGURE 3.9: Diagram of the sample mount.

4. EXPERIMENTAL RESULTS

4.1. Calibration with 1737

A Corning 1737 substrate, a well characterized thermal standard, was measured to verify the validity of the 3ω method and the accuracy of our testing equipment. Corning 1737 is a boro-aluminosilicate glass with room temperature thermal conductivity of 0.91 W m^{-1} K^{-1} and thermal diffusivity 0.504 mm^2 s^{-1} [22]. Figure 4.1. shows an example of experimental data [23] gathered on a 1737 substrate; in this figure, the 3ω voltage data has been converted to thermal resistance. A fit to the data using the 2D heater model is also plotted. The fitting procedure is simple; since there are only two free parameters (κ and D) and the linear region of the ΔR_{th} *vs.* f plot is independent of the diffusivity, the slope of the linear region is used to calculate the conductivity using Equation 2.30. The rest of the data (i.e., the magnitude of the low frequency data and the behavior of the high frequency data) is then fitted using the only remaining free parameter, D. Using this process, the measured thermal conductivity and diffusivity of the 1737 substrate is 0.90 W m^{-1} K^{-1} (1.1% error) and 0.7 mm^2 s^{-1} (40% error) respectively. This result shows that for low-κ and low-D bulk materials, our measurement system provides an accurate measurement of the thermal conductivity. Thermal diffusivity measurements are less accurate, but can serve as an order of magnitude estimate or as a confirmation of diffusivity measurements with other techniques.

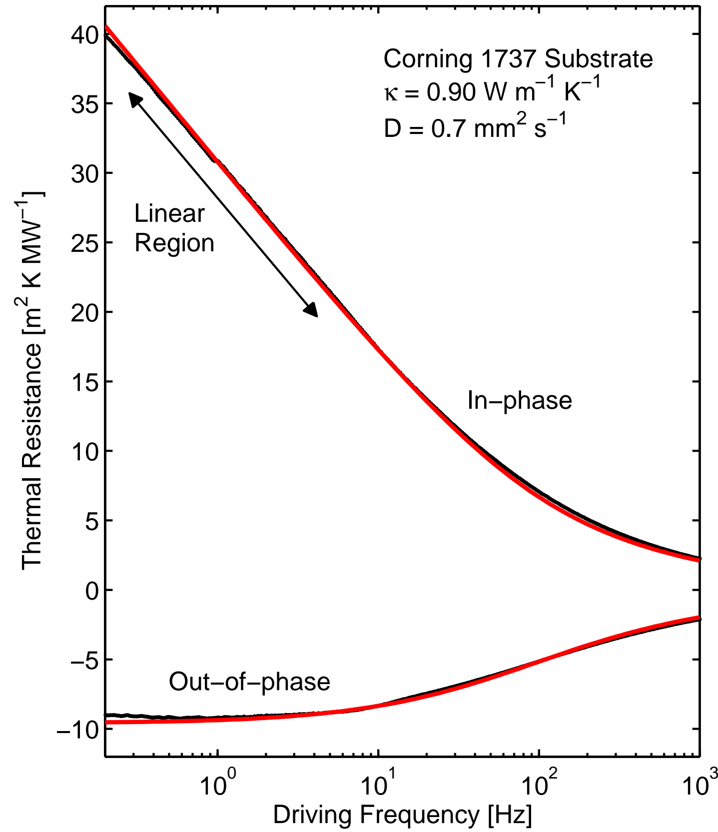

FIGURE 4.1: Thermal resistance *vs.* current frequency for a measurement on a 1737 substrate. Fitting of the data (black line) to the 2D heater model (red line) yields a measured thermal conductivity of 0.90 W m^{-1} K^{-1} and thermal diffusivity of 0.7 mm^2 s^{-1}.

4.2. Effects of Doping on Si

As reported in [23], the thermal conductivity is also measured for two types of (100)-oriented silicon substrates: a n-type, As-doped Si with electrical resistivity 0.0010 Ω cm and a p-type, B-doped Si with electrical resistivity 50 Ω cm. In this experiment, several substrates of both doping concentrations are tested with heater widths ranging from 10-20 μm.; these substrates have AlPO films of various thicknesses ($<$ 200 nm). Since these films

are thin, they will not affect the slope of the in-phase R_{th} *vs.* f curves, so the 1D model is used to extract the substrate thermal conductivity. As the thermal diffusivity of silicon is high (on the order of 80 mm^2 s^{-1}) [24], the linear region extends past the range of the lock-in amplifier; thus, is it not possible to obtain high frequency data about the thermal diffusivity.

Figure 4.2. shows the in-phase R_{th} *vs.* f data for both an n- and p-Si substrate, using similar measurement conditions. Again, it is important to note that only the slope of the data is meaningful here. The slope of the n-Si data is steeper than that of the p-Si, indicating that it has a lower thermal conductivity. This is consistent with the lower electrical resistivity (larger carrier concentration) of the n-Si compared to the p-Si (see Figure 4.2. for the relationship between carrier concentration and the electrical resistivity of both n-Si and p-Si).

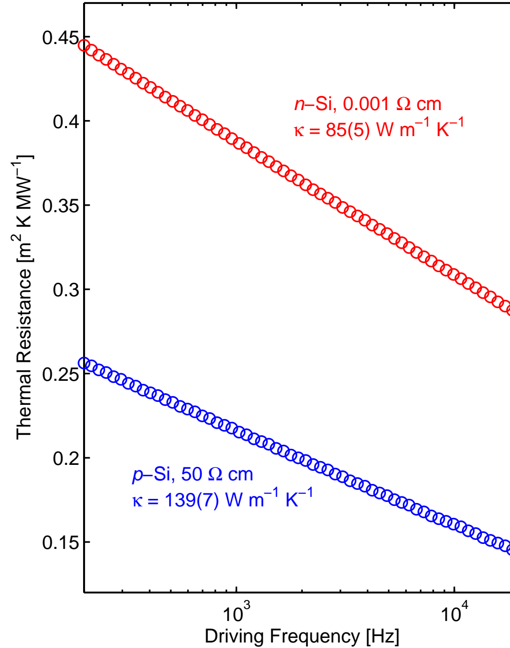

FIGURE 4.2: Thermal resistance *vs.* current frequency for n-Si and p-Si.

From multiple measurements of both types of Si, we determine that the thermal

conductivity of the p-Si and n-Si is 139(7) W m^{-1} K^{-1} and 85(5) W m^{-1} K^{-1} respectively. Here, the measurement uncertainty represents the standard deviation of the measured conductivities. This data indicates that the two types of silicon possess very different thermal conductivities. In particular, the p-type substrates, which have a significantly higher electrical resistivity (lower carrier density) than the n-type substrates, also have a much higher thermal conductivity than the n-Si. Figure 4.2. shows the relationship between electrical resistivity and electrical carrier density for n- and p-type silicon; clearly, as the resistivity increases, the carrier density decreases for both dopant types. From Figure 4.2., we estimate that the p-Si and n-Si have carrier densities of 3×10^{14} cm^{-3} and 6×10^{19} cm^{-3}. and If the thermal transport properties of the silicon were dominated by charge carriers, the thermal conductivity would increase with decreasing electrical resistivity (increasing carrier density). This is in contradiction to our data, suggesting that, at room temperature, the thermal properties of silicon is dominated by phonon transport rather than electron transport. By adding additional charge carriers to the the crystal, increased phonon-charge scattering events lead to lower thermal conductivity. This conclusions is supported by the experimental work of Rowe and Bhandari [25], which shows that at high temperature (tens to hundreds of Kelvin, depending on the type of silicon), the thermal conductivity decreases with increasing temperature. This is a result of the increasing number of available charge carriers with increasing temperature. From [25], the thermal conductivity of p-Si with carrier density 4.2×10^{14} cm^{-3} is 155 W m^{-1} K^{-1} For n-Si carrier concentration interpolated between carrier densities of 2×10^{19} cm^{-3} and 17×10^{19} cm^{-3} is 90 W m^{-1} K^{-1}. This is in reasonable agreement with our data, with percent differences of 7.5% (5.6%) for the p-Si (n-Si). This result shows that our measurement system is capable of measuring high-κ bulk materials. However, we are not able to measure the thermal diffusivity of silicon and other high-D materials as the linear region extends outside the system's upper frequency range. As discussed in Section 2.4,

using a significantly wider heater can move the 2D heater effects to a lower frequency within the range of our circuitry, allowing for measurements of the diffusivity.

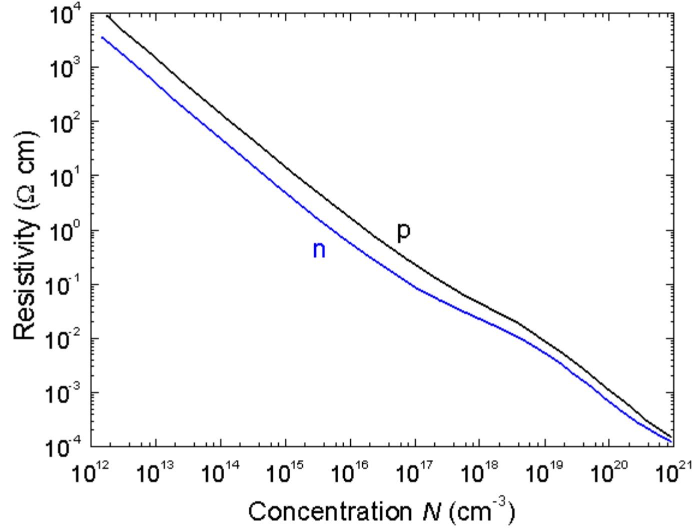

FIGURE 4.3: Electrical resistivity *vs.* carrier density for n- and p-type Si. From [26]

4.3. AlPO Thin Films

4.3.1 Sample Preparation

Amorphous AlPO thin films with stoichiometry $Al_2P_{1.2}O_6$ were produced via a solution deposition process detailed in [23, 27]. The films were deposited on silicon substrates with a native oxide layer. The thickness of the films can be varied by changing the concentration of the AlPO precursor solutions or by deposition additional films layers. For this experiment, multiple series of 1-, 2-, 3-, and 4- layer films were deposited. After all layers are deposited, the samples are annealed in air at either 450 °C or 600 ° C for 30 minutes to drive off any remaining solution from the film.

As the film thickness is an important parameter in the thermal conductivity measurements, the thickness of each sample was carefully measured using a J.A. Woollam Co.,

Inc. M2000X-210 ellipsometer (see Figure 4.4 for an example measurement on several film thicknesses). For each film, the ellipsometry measurement was performed at incident angles 55°, 60°, and 65°. The thickness of the films were determined using an iterative fitting process, using a Cauchy model that incorporated both the effects of the silicon substrate and the native oxide layer beneath the AlPO film.

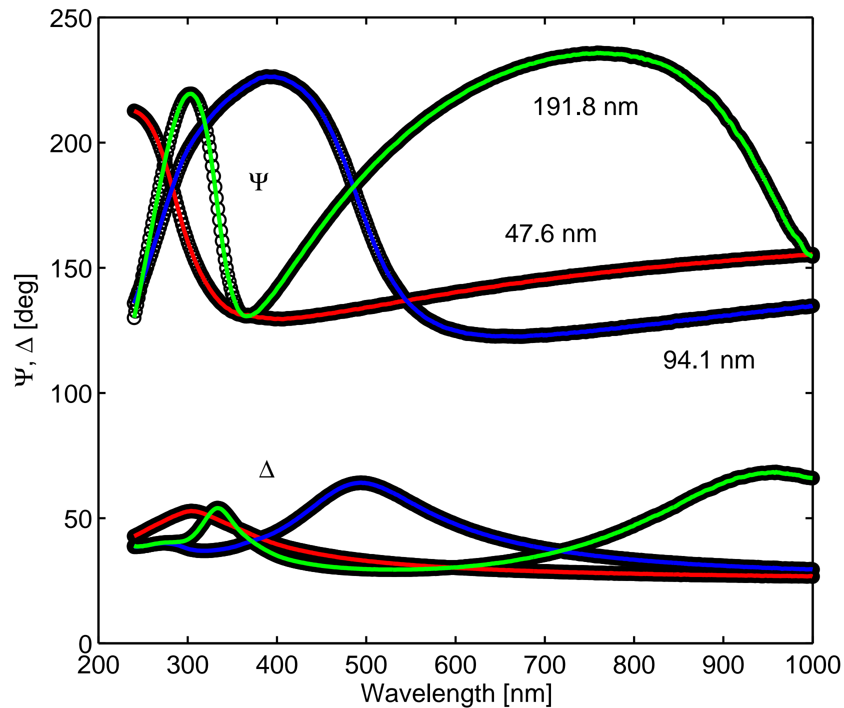

FIGURE 4.4: Ellipsometry measurements on 1-, 2-, and 4-layer AlPO films at an incident angle of 65°. Points are data and lines are fits to the data using a Cauchy model.

Figure 4.5 shows the results of the thickness measurements on two series of AlPO films annealed at two different temperatures. The linear behavior of the data indicates that each film layer is approximately the same thickness. Also, the films annealed at 600 °C are systematically thinner than their 450 ° C counterparts.

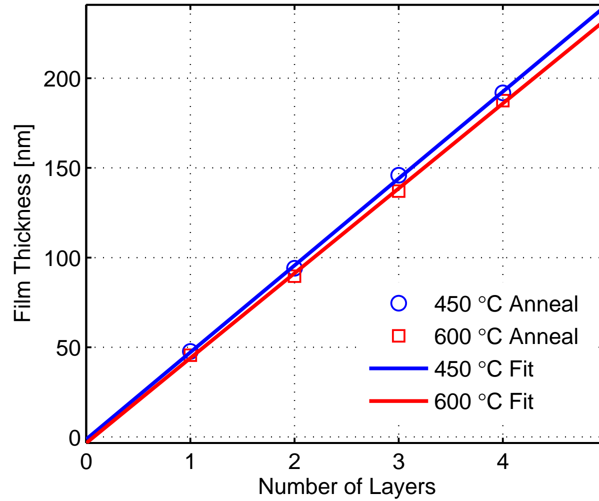

FIGURE 4.5: Thickness *vs.* number of layers of the 450°C and 600 °C annealed AlPO films. The linear behavior shows that each layer has approximately the same thickness. The films annealed at 600 °C are slightly thinner than their 450 °C counterparts.

To verify the accuracy of the ellipsometry measurements, the thickness of the single layer films were also characterized using the x-ray reflectivity (XRR) technique on a Bruker D8 Discover diffractometer (see Figure 4.6). XRR measurements confirmed the ellipsometry measurements to within 1%. Thickness measurements are extracted from the XRR data by measuring the angular distance between adjacent intensity fringes.

4.3.2 Thermal Conductivity Results

Figure 4.7 plots both the thermal resistance *vs.* frequency curves for AlPO samples of different thickness and the corresponding the values for ΔR_{th} against the film thickness. This measurement consists of a series of four films annealed at 600 °C on *p*-Si substrates. As expected, the addition of a thin film adds a frequency independent increase ΔR_{th} to the in-phase thermal resistance. Thicker films create a larger thermal resistance. Only the in-phase data is shown as the out of phase-data does not yield any information about the films (in this frequency region, the out-of-phase data is independent of frequency and film thickness). For reference, the 2D heater model for the silicon substrate is plotted along

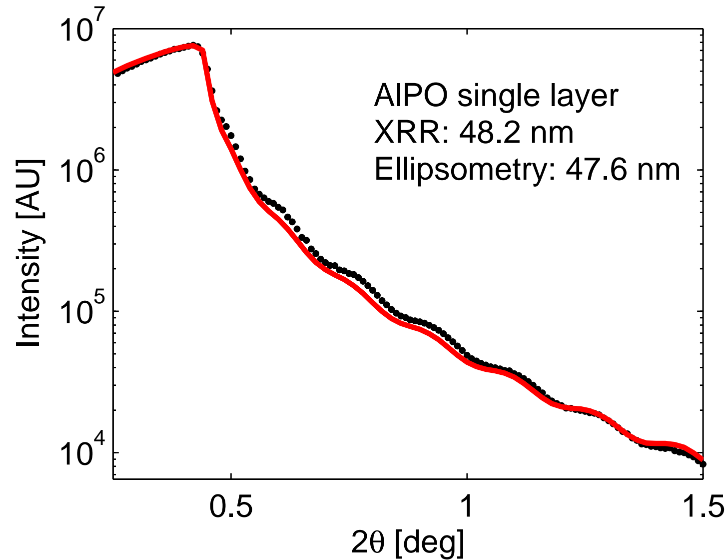

FIGURE 4.6: XRR measurement on a single layer AlPO film.

with the data. This model uses the measured thermal conductivity of the substrate and an estimated thermal diffusivity of 88 $\mathrm{mm}^2\ \mathrm{s}^{-1}$. The number used for this diffusivity does not affect the extracted film thermal conductivity, but it does affect the zero thickness intercept value for ΔR_i. For the measurements on the AlPO films, $\Delta R_i = 34\ \mathrm{m}^2\ \mathrm{K}\ \mathrm{GW}^{-1}$; this is due to the thermal resistance present at both the substrate/film and film/heater interfaces, as well as any error in the value used for the substrate thermal diffusivity. The linear behavior of the data suggests that in this thickness regime, the thermal conductivity is independent of film thickness. Thus, the film thermal conductivity can be extracted from the inverse slope of a linear fit to this data. Using this method, we obtain 0.94(3) W $\mathrm{m}^{-1}\ \mathrm{K}^{-1}$ for the thermal conductivity of the AlPO films. Additionally, we do not see any difference in the thermal conductivity of the samples annealed at different temperatures.

It is useful to compare the measured thermal conductivity of AlPO to other amorphous oxides. Panzer *et al.* [28] report a thickness depend thermal conductivity of HfO_2 films of 0.49 - 0.95 W $\mathrm{m}^{-1}\ \mathrm{K}^{-1}$ for films of thickness 6 20 nm. Gabriel and Talghader [29] measure the thermal conductivity of 50-100 nm thermally grown SiO_2 as 1.5 -1.6 W

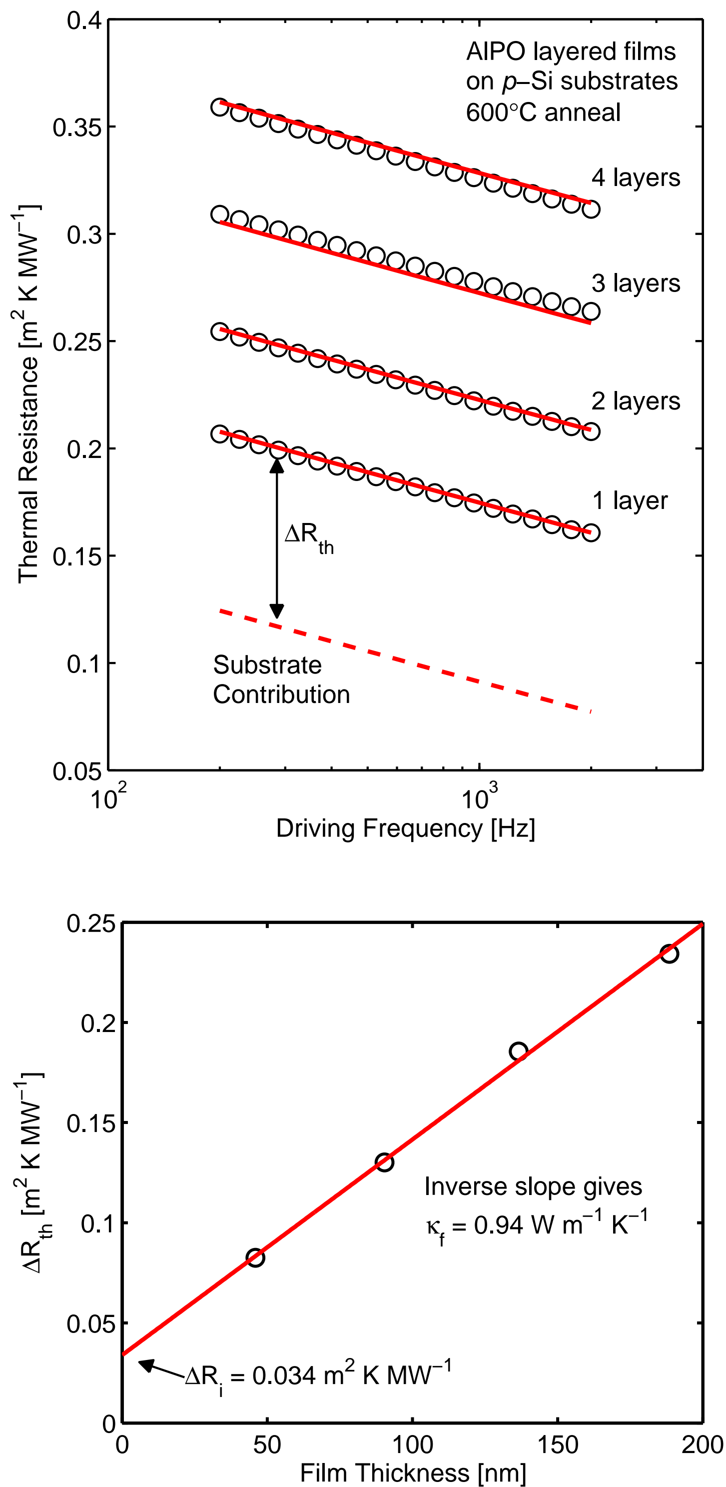

FIGURE 4.7: Top: Thermal resistance *vs.* current frequency for a series of AlPO films on p-Si. Bottom: ΔR_{th} *vs.* d_f for a series of AlPO films on p-Si. The non-zero resistance intercept at $d_f = 0$ is caused by parasitic thermal resistance R_i at the substrate/film and film/heater interfaces.

m^{-1} K^{-1}, of 100-nm HfO_2 as 1.72 W m^{-1} K^{-1}, and 100-nm Al_2O_3 as 2.59 W m^{-1} K^{-1}. Amorphous AlPO films are therefore in a similar thermal conductivity regime as these other common materials.

Kim *et al.* [9] reports thermal interface resistances of 18 m^2 K GW^{-1} for SiO_2 films on Si grown using a steam/dry oxidation method. Panzer *et al.* [28] report thermal interface resistances in the range of 3-12 m^2 K GW^{-1} for their $HfO_2/SiO_2/Si$ stacks. Our result of 34 m^2 K GW^{-1} for the AlPO/SiO_2/Si stacks is larger than both of these. However, there is the possibility for significant error in this measurement as it includes the unknown thermal resistance of the heater/film interface, which is potentially quite large. In addition, any error in the numbers used for the also unknown thermal diffusivity of the silicon substrates propagates into this measurement. In order to more accurately measure the thermal resistance of the film/substrate interface, more work must be done to quantify the heater/film interface and to determine the substrate diffusivity.

5. CONCLUSIONS

In this thesis, a system designed to measure thermal conductivity via the 3ω method was constructed. This system can measure the thermal conductivity of both bulk and thin film materials. Thermal diffusivity measurements on bulk materials can also be performed, but these measurements are limited to low diffusivity materials due to the limited frequency range of system. Several materials were tested, including Corning 1737, a well known thermal calibration standard. Results on bulk 1737 with our system agree with Corning's results [22] to within 2% for thermal conductivity and within 40% for thermal diffusivity. The model used to calculate the bulk thermal conductivity is independent of the diffusivity measurements.

A lift-off process was developed to construct high quality microheaters onto the surface of samples. This process uses UV photolithography to create a patterned photomask on the surface of each sample. Thermal evaporation is then used to deposit the metal for the heater. The photomask and excess metal are removed via sonication in organic solvents. With this method, we have made rectangular heaters of dimensions 1 mm by 5 μm, with variations in heater width less than 1 μm.

Automation software for the measurement system was developed within the LabVIEW framework. This system automates the data gathering aspect of the measurement by communicating with the electronic measurement equipment to make voltage measurements with a lock-in amplifier and a digital oscilloscope over a wide range of input frequencies. The software uses custom signal stabilization routines to ensure that the lock-in reading has properly stabilized before recording data.

The developed equipment was used to measure the thermal conductivity of solution deposited amorphous AlPO thin films on silicon substrates. A technique similar to that used by Kim *et. al* [9] was used to isolate the film's thermal conductivity from the effects

caused by the substrate and any parasitic thermal interfaces. From these measurements, we determined that the AlPO films have a thermal conductivity of 0.94(3) W m^{-1} K^{-1}, similar to other amorphous oxides.

In addition, we tested multiple series of AlPO films on two different types of silicon substrates. Our results confirmed that the measured film thermal conductivity is indeed independent of the type of substrate used. The data from these measurements was also used to calculate the thermal conductivity of the bulk silicon. We found that silicon lightly doped p-type has a thermal conductivity of 139(7) W m^{-1} K^{-1} while silicon more heavily doped n-type has a thermal conductivity of 85(5) W m^{-1} K^{-1}. These results are in reasonable agreement with those shown by Rowe and Bhandari [25].

In the future, characterization of many other material types with the 3ω measurement system is possible. In addition to dielectric thin films, films that are electrically conducting are of particular interest. New material classes such as amorphous metals and ferecrystals are especially well suited to this technique as they generally exhibit much lower thermal conductivity than traditional metals and semiconductors. However, there are additional challenges that these measurements pose; for example, the metallic heater used in these experiments cannot be placed directly on the surface of a conducting film. To overcome this, an addition insulating film must be deposited between the film of interest and the heater. If the thickness of this film is constant from sample to sample, the thin film technique used here can be used without modification for conductive samples. The thermal resistance of the insulating film is absorbed by the thermal interface resistance offset.

High and low temperature measurements are also of interest. The substrate heater used in the TCR measurements was designed with this in mind; the cartridge heaters themselves can provide enough power to heat the copper block to sufficiently high temperatures. High temperature measurements must be done *in situ* to reduce oxidation of

the samples and heaters as oxidation of the films may change their thermal properties and oxidation of the heaters will result in an altered resistivity and TCR. It may also be useful to use a metal with better high temperature stability than aluminum (e.g. platinum). For low temperature measurements, the heaters can be removed and the copper block immersed in liquid nitrogen/helium, providing cooling to the sample.

BIBLIOGRAPHY

1. Kim, W., Zide, J., Gossard, A., Klenov, D., Stemmer, S., Shakouri, A., and Majumdar, A. *Phys. Rev. Lett.* **96**, 045901 Feb (2006).

2. Sutton, A. P. *Electronic Structure of Materials*. Oxford University Press, first edition, (1993).

3. Cowell, E. W. *Electronic device and nanolaminate application of amorphous metal thin films*. PhD thesis, Oregon State University, April (2012).

4. Cahill, D. G. and Pohl, R. O. *Phys. Rev. B* **35**, 4067–4073 Mar (1987).

5. Birge, N. O. and Nagel, S. R. *Phys. Rev. Lett.* **54**, 2674–2677 Jun (1985).

6. Birge, N. O. and Nagel, S. R. *Review of Scientific Instruments* **58**(8), 1464–1470 (1987).

7. Cahill, D. G. *Review of Scientific Instruments* **61**(2), 802–808 (1990).

8. Cahill, D. G., Katiyar, M., and Abelson, J. R. *Phys. Rev. B* **50**, 6077–6081 Sep (1994).

9. Kim, J. H., Feldman, A., and Novotny, D. *Journal of Applied Physics* **86**(7), 3959–3963 (1999).

10. Borca-Tasciuc, T., Kumar, A. R., and Chen, G. *Review of Scientific Instruments* **72**(4), 2139–2147 (2001).

11. Battaglia, J.-L., Wiemer, C., and Fanciulli, M. *Journal of Applied Physics* **101**(10), 104510 (2007).

12. Zong, Z.-X., Qiu, Z.-J., Zhang, S.-L., Streiter, R., and Liu, R. *Journal of Applied Physics* **109**(6), 063502 (2011).

13. Ramu, A. T. and Bowers, J. E. *Journal of Applied Physics* **112**(4), 043516 (2012).

14. Raudzis, C. E., Schatz, F., and Wharam, D. *Journal of Applied Physics* **93**(10), 6050–6055 (2003).

15. Jacquot, A., Vollmer, F., Bayer, B., Jaegle, M., Ebling, D., and Bttner, H. *Journal of Electronic Materials* **39**, 1621–1626 (2010).

16. Abramowitz, M. and Stegun, I. *Handbook of Mathematical Functions*. Dover Publications, ninth edition, (1970).

17. http://en.wikipedia.org/wiki/Electrical_resistivity_and_conductivity. Accessed April 23, 2013.

18. http://www.ohmite.com/cat/res_tch35.pdf. Accessed March 20, 2013.

19. Kimling, J., Martens, S., and Nielsch, K. *Review of Scientific Instruments* **82**(7), 074903 (2011).

20. http://www.thinksrs.com/downloads/PDFs/Catalog/SR850c.pdf. Accessed May 10, 2013.

21. http://www.thinksrs.com/downloads/PDFs/ApplicationNotes/AboutLIAs.pdf. Accessed May 10, 2013.

22. http://www.vinkarola.com/pdf/Corning%20Glass%201737%20Properties.pdf. Accessed May 10, 2013.

23. Wiedle, R. A., Warner, M., Plassmeyer, P. N., Page, C. J., and Tate, J. *Manuscript submitted to Thin Solid Films* (2013).

24. http://www.ioffe.ru/SVA/NSM/Semicond/Si/thermal.html. Accessed May 10, 2013.

25. Rowe, D. M. and Bhandari, C. M. *Prog. Cryst. Growth and Charact.* **13** (1986).

26. http://www.ioffe.rssi.ru/SVA/NSM/Semicond/Si/Figs/135.gif. Accessed May 10, 2013.

27. Meyers, S. T., Anderson, J. T., Hong, D., Hung, C. M., Wager, J. F., and Keszler, D. A. *Chemistry of Materials* **19**(16), 4023–4029 (2007).

28. Panzer, M. A., Shandalov, M., Rowlette, J., Oshima, Y., Chen, Y. W., McIntyre, P. C., and Goodson, K. E. *Electron Device Letters, IEEE* **30**(12), 1269–1271 (2009).

29. Gabriel, N. T. and Talghader, J. J. *Journal of Applied Physics* **110**(4), 043526 (2011).